RESEARCH ARTICLE

Key Points:
- Two coupled GCMs require multiple millennia to equilibrate to a gradual CO_2 doubling and have an ECS ~1 K larger than IPCC estimates
- For the majority of both runs the feedback parameter is near constant, but much smaller than seen following an instantaneous CO_2 quadrupling
- Intermodel and temporal differences in feedback parameter are tied to differences in lower atmospheric stability and the vertical velocity

Supporting Information:
- Supporting Information S1

Correspondence to:
D. Paynter,
david.paynter@noaa.gov

Equilibrium Climate Sensitivity Obtained From Multimillennial Runs of Two GFDL Climate Models

D. Paynter[1] (iD), T. L. Frölicher[2,3], L. W. Horowitz[1] (iD), and L. G. Silvers[1,4] (iD)

[1]Geophysical Fluid Dynamics Laboratory, Princeton, NJ, USA, [2]Climate and Environmental Physics, Physics Institute, University of Bern, Bern, Switzerland, [3]Oeschger Centre for Climate Change Research, University of Bern, Bern, Switzerland, [4]Program in Atmospheric and Oceanic Sciences, Princeton University, Princeton, NJ, USA

Abstract Equilibrium climate sensitivity (ECS), defined as the long-term change in global mean surface air temperature in response to doubling atmospheric CO_2, is usually computed from short atmospheric simulations over a mixed layer ocean, or inferred using a linear regression over a short-time period of adjustment. We report the actual ECS from multimillenial simulations of two Geophysical Fluid Dynamics Laboratory (GFDL) general circulation models (GCMs), ESM2M, and CM3 of 3.3 K and 4.8 K, respectively. Both values are ~1 K higher than estimates for the same models reported in the Fifth Assessment Report of the Intergovernmental Panel on Climate Change obtained by regressing the Earth's energy imbalance against temperature. This underestimate is mainly due to changes in the climate feedback parameter ($-\alpha$) within the first century after atmospheric CO_2 has stabilized. For both GCMs it is possible to estimate ECS with linear regression to within 0.3 K by increasing CO_2 at 1% per year to doubling and using years 51–350 after CO_2 is constant. We show that changes in $-\alpha$ differ between the two GCMs and are strongly tied to the changes in both vertical velocity at 500 hPa (ω_{500}) and estimated inversion strength that the GCMs experience during the progression toward the equilibrium. This suggests that while cloud physics parametrizations are important for determining the strength of $-\alpha$, the substantially different atmospheric state resulting from a changed sea surface temperature pattern may be of equal importance.

1. Introduction

How sensitive is Earth's surface air temperature to a change in radiative forcing? The answer to this question is usually provided in terms of the equilibrium climate sensitivity (ECS), defined as the change in global mean surface air temperature that arises once the physical climate system has equilibrated to a doubling of atmospheric CO_2 (e.g., Knutti & Hegerl, 2008). Because the climate system requires millennia to reach equilibrium, it is computationally expensive to estimate ECS with comprehensive climate models. As a result, various computationally cheaper methods have been used to estimate ECS from shorter simulations.

One common method, detailed by Gregory et al. (2004), is to run the general circulation model (GCM) for order of a hundred years under a fixed radiative forcing (F) and regress the change in the net downward top-of-atmosphere radiative flux (N) against the change in surface air temperature (T), where it is assumed that the energy balance at the top of atmosphere is satisfied by $N = F - \alpha T$. The slope of this regression is the climate feedback parameter, denoted as $-\alpha$ (in W m^{-2} K^{-1}). The temperature intercept at $N = 0$ W m^{-2} is the estimated ECS. This method, referred to here as the linear extrapolation (LE) method, was used to diagnose ECS in the Fifth Assessment Report of the Intergovernmental Panel on Climate Change (IPCC-AR5) (Andrews et al., 2012; Flato et al., 2013).

To date, few GCMs are run for more than a thousand years under increased atmospheric CO_2 (Danabasoglu & Gent, 2009; Gregory et al., 2004; Jonko et al., 2012; Li et al., 2012; Senior & Mitchell, 2000; Stouffer & Manabe, 1999, 2003) and only a few studies have investigated the change in $-\alpha$ as equilibrium is approached. Senior and Mitchell (2000) and Gregory et al. (2004), for example, used millennial simulations of the HadCM model to show that most of the change in $-\alpha$ occurs within the first few hundred years following an increase of CO_2, after which $-\alpha$ remains fairly constant. However, the GCM was still out of equilibrium at the end of these runs, so it was not possible to determine the true ECS of either model. Indeed, when ECHAM5/MPIOM was run to equilibrium (Li et al., 2012), $-\alpha$ abruptly increased after the model was already 80% to equilibrium. Thus, it remains unclear if and how $-\alpha$ changes as the system approaches equilibrium, and over which time periods the LE method provides accurate estimates of ECS.

The results from two coupled climate models developed at the Geophysical Fluid Dynamics Laboratory (GFDL) are used in this study: the GFDL CM3 (Donner et al., 2011; Griffies et al., 2011) and the GFDL ESM2M (Dunne et al., 2012, 2013). Both models participated in the Coupled Model Intercomparison Project Phase 5. In this paper, we present two new multimillennial simulations of CM3 (4,800 years) and ESM2M (4,430 years) following a 1% per year increase in atmospheric CO_2 to doubling. These long runs therefore give us the opportunity to know the true ECS of both GCMs rather than relying upon techniques that estimate ECS from shorter 150 to 300 year runs in which CO_2 has been quadrupled (e.g., Andrews et al., 2012, 2015; Armour, 2017; Geoffroy, Saint-Martin, Olivié, et al., 2013; Proistosescu & Huybers, 2017; Winton, Adcroft, et al., 2013). These shorter runs have resulted in a range of estimates of ECS for these two models. For instance, Andrews et al. (2012) applied the LE method to the first 150 years following an instantaneous quadrupling of CO_2 and estimated ECS values of 2.4 K and 4.0 K for ESM2M and CM3, respectively. However, Winton, Adcroft, et al. (2013) applied the LE method to the last 160 years of extended 300 year versions of these quadrupling of CO_2 runs to obtain much larger ECS estimates of 3.2 K and 4.6 K, respectively. Thereby raising the questions of what is the true ECS of these models and over which time periods should the LE method be applied? In section 3 we focus on the evolution of the top of atmosphere imbalance, N, and surface air temperature, T, and accordingly $-\alpha$, as the models approach true equilibrium in these new long runs, so to allow us to evaluate time periods over which the LE method provides accurate estimates of ECS.

Despite the relative lack of forced millennial length runs of GCMs, numerous studies have now reported that the magnitude of $-\alpha$ is not invariant for a particular GCM (Andrews et al., 2015; Armour, 2017; Armour et al., 2016, 2013; Feldl et al., 2014; Frölicher & Paynter, 2015; Frölicher et al., 2014; Gettelman et al., 2012; Haugstad et al., 2017; He et al., 2017; Kay et al., 2012; Knutti & Rugenstein, 2015; Meraner et al., 2013; Murphy, 1995; Paynter & Frölicher, 2015; Rugenstein, Caldeira, et al., 2016; Rugenstein, Gregory, et al., 2016; Senior & Mitchell, 2000; Trossman et al., 2016; Winton, Adcroft, et al., 2013; Winton, Griffies, et al., 2013; Winton et al., 2010). These changes in $-\alpha$ have been largely attributed to changes in the sea surface temperature (SST) pattern (e.g., Andrews & Webb, 2017; Andrews et al., 2015; Gregory & Andrews, 2016; Senior & Mitchell, 2000; Williams et al., 2008; Zhou et al., 2016, 2017), changes in the ocean heat uptake pattern (Frölicher et al., 2014; Gregory & Andrews, 2016; He et al., 2017; Rose et al., 2014; Rose & Rayborn, 2016; Rugenstein, Caldeira, et al., 2016; Rugenstein, Gregory, et al., 2016; Winton et al., 2010; Winton, Adcroft, et al., 2013; Winton, Griffies, et al., 2013), or changes in the type of forcing agent (Hansen, 2005; Marvel et al., 2016; Paynter & Frölicher, 2015; Shindell, 2014; Shindell et al., 2010). A recent study by Haugstad et al. (2017) suggests some synthesis between these views and demonstrates that regardless of the cause (i.e., differences in ocean heat uptake pattern or differences in forcing agent pattern), the resulting change in SST pattern is ultimately the determining factor of the changes to $-\alpha$.

Although the changes in SST and sea ice concentration may be the driving influence of the change in $-\alpha$, the atmospheric response itself must ultimately be the result of a change in a radiatively active component of the atmosphere (i.e., clouds, water vapor, and temperature structure). Indeed, several studies have linked change in $-\alpha$ to change in the shortwave cloud feedbacks (e.g., Andrews et al., 2015; Haugstad et al., 2017; Paynter & Frölicher, 2015; Senior & Mitchell, 2000; Williams et al., 2008). Despite this, much of the focus in the literature thus far (Armour et al., 2016; Rose et al., 2014; Rugenstein, Gregory, et al., 2016; Winton, Griffies, et al., 2013) has been on understanding the role of the ocean circulation change in determining the SST pattern. Only recently have studies begun to focus on quantifying the influence of SST pattern upon the state of the atmosphere in which the cloud feedbacks occur (Andrews & Webb, 2017; Ceppi & Gregory, 2017; Gregory & Andrews, 2016; Rose & Rayborn, 2016; Silvers et al., 2017; Zhou et al., 2016).

This is not to say that there is a lack of literature on linking differences in cloud feedbacks to differences in the atmospheric physics parameterizations. For example, studies have pointed to the importance of convection schemes for determining the strength of atmospheric feedbacks (Sherwood et al., 2015, 2014; Webb et al., 2012, 2015; Zhao et al., 2016). These studies have generally employed the philosophy that each GCM can be represented by a single value of $-\alpha$, and thus, the differences between the GCMs can be defined by differences in the atmospheric physics parameterizations. Such an approach is not problematic when all GCMs are forced with the same SST perturbations (e.g., Zhao et al., 2016). However, in the case of coupled model runs, a difference in $-\alpha$ between two models will potentially be the result of both differences in the SST pattern and differences in the atmospheric cloud physics parameterizations.

In section 4 we investigate the regional contributions to $-\alpha$ in the two multimillennial runs to show how the evolving SST pattern influences the spatial pattern of various feedbacks. We also look at the evolution in the spatial pattern of two metrics of importance for understanding changes in clouds; vertical velocity at 500 mb ($\Delta\omega_{500}$) and estimated inversion strength (EIS). This primarily allows us to see how changes in the SST pattern can be linked to changes in the atmospheric state, which in turn would explain changes in the cloud feedback pattern. Studies have shown (e.g., Bony et al., 2004; Bony & Dufresne, 2005; Brient & Bony, 2013) that changes in ω_{500} over the tropical oceans can be a useful predictor of regional changes in the longwave cloud radiative effect (LWCRE) and shortwave cloud radiative effect (SWCRE) resulting from middle and high cloud cover changes. For example, an increase in upward vertical velocity (a negative change in ω_{500}) is associated with increased convection and thereby increased high cloud amount, which in turn indicates a negative change in SWCRE and positive LWCRE.

It is less apparent how important ω_{500} is in the middle and high latitudes, where convection plays a lesser role in determining cloud behavior. In these regions, lower-tropospheric stability may be of greater significance. For example, if SSTs in a particular region, such as the Southern Ocean, warm slower than the middle troposphere, the atmospheric stability will increase and induce a negative shortwave cloud feedback through increased low cloud cover (Andrews et al., 2015; Senior & Mitchell, 2000; Williams et al., 2008). EIS (Wood & Bretherton, 2006) has been used to connect changes in cloud feedbacks under climate change to vertical stability (Qu et al., 2015; Rose & Rayborn, 2016; Zhou et al., 2016). Wood and Bretherton (2006) proposed EIS as a metric to explain the presence of stratocumulus cloud deck regions, such as those near the west coasts of Peru and California. However, recent work (Andrews & Webb, 2017; Rose & Rayborn, 2016; Zhou et al., 2016, 2017) has suggested that EIS can be applied in a more general sense over most ocean regions, as a measure of how atmospheric stability alters low level cloud feedbacks as the ocean heat uptake pattern (i.e., the SST pattern) evolves in response to forcing. Accordingly, in section 4 we investigate how useful EIS and ω_{500} are for explaining the evolution in SWCRE and LWCRE as both models head toward equilibrium (section 4.3). We propose the EIS-ω_{500} space occupied by the two GCMs aids in understanding the importance of SST pattern versus atmospheric physics parametrizations for determining differences in $-\alpha$ (section 4.4).

2. Methods

CM3 and ESM2M share near-identical ocean models based upon GFDL MOM5. This makes a comparison of long runs between CM3 and ESM2M models especially interesting, as differences in the climate response can be attributed to differences in their respective atmospheric models, AM3 and AM2.1. Because AM3 was developed from the code base of AM2.1, many components are either identical or only slightly different (e.g., the planetary boundary layer, gravity wave drag, radiation, and cloud optics schemes). However, both the stratiform and convective clouds schemes were significantly updated in AM3 compared to AM2.1 (Donner et al., 2011). AM3 also has a prognostic cloud droplet number scheme based upon aerosol activation and a fully interactive chemistry scheme, neither of which were present in AM2.1. In this paper we do not attempt to diagnose which of these changes are most important for the differing response of the GCMs, although the very different cloud responses between the models that we document in section 4 point to the importance of the aforementioned updates to the cloud schemes.

For both models, we prescribe atmospheric CO_2 to increase from a preindustrial level (286 ppmv) by 1%/yr until doubling (572 ppmv), after which the CO_2 concentration is held fixed. We refer to these runs as the 2XS runs, the "S" to signify that CO_2 was increased at a slow rate rather than instantaneously. Note that unless stated otherwise "year 1" refers to the first year in which CO_2 is constant.

We also make use of simulations with the same models in which CO_2 has been instantaneously quadrupled (4XI). These simulations are identical to those submitted to Coupled Model Intercomparison Project Phase 5 but have been run for a further 150 years, making them 300 years long in total (Winton, Adcroft, et al., 2013). Finally, we make use of an 11-member ensemble of 10 year 4XI runs of CM3. We also use companion 20 year runs of AM2.1 and AM3 (the atmospheric components of ESM2M and CM3, respectively), in which CO_2 is doubled or quadrupled, but SSTs are held fixed.

T is defined as the difference in global mean surface air temperature between the experiment (i.e., with all radiative forcing agents other than CO_2 set to 1,860 levels) and a preindustrial control run (i.e., with all

radiative forcing agents set to 1,860 levels). For example, T_{350} denotes the difference in temperature between the experiment and control 350 years after CO_2 is fixed. The same convention also holds for the top-of-atmosphere imbalance; N, T_{FSST}, and N_{FSST} are defined as the difference between the fixed SST experiments with and without the CO_2 increase, averaged over a 20 year period.

The progression to equilibrium of the 2XS runs is split into three time periods. For each period we estimate ECS (i.e., $T(N = 0$ W m$^{-2})$) and the radiative forcing F (i.e., $(N(T = 0$ K$))$ assuming that the $-\alpha$ obtained for that period can be used to extrapolate the behavior of the model to the limits of $N = 0$ and $T = 0$. The first period (P1) includes the increase in CO_2 and the first 10 years when CO_2 is constant (i.e., $\Delta T_{P1} = T_{10}$). The next two periods split the subsequent progression to equilibrium into two roughly equal ΔT changes (~1.0 K for ESM2M and ~1.25 K for CM3). Period 2 (P2) covers years 11 to 350 after CO_2 is fixed (i.e., $\Delta T_{P2} = T_{350} - T_{11}$), and period 3 (P3) covers the years 351 to equilibrium (year 2500 for ESM2M and year 4800 for CM3).

During periods 2 and 3 (and other intervals when CO_2 is constant), it is possible to apply the LE method to estimate ECS with $-\alpha$ defined as the gradient of the fit over that period. Due to the changing forcing, it is not possible to use the LE method in period 1 to obtain $-\alpha$. Instead, we extrapolate in N and T space between the fully coupled GCM 10 years after CO_2 doubling is reached and the fixed SST version of the GCM in which CO_2 has also been doubled. Hence, $-\alpha_{P1}$ is defined as

$$-\alpha_{P1} = \frac{\Delta N_{P1}}{\Delta T_{P1}} = \frac{N_{10} - N_{FSST}}{T_{10} - T_{FSST}} \sim \frac{N_{10} - N(T = 0 \text{ K})}{T_{10}}, \tag{1}$$

where T_{10} and N_{10} are calculated as an average between years 1 and 20 (after CO_2 doubling is reached) of the 2XS runs and T_{FSST} and N_{FSST} are the global mean change in T and N averaged over 20 years in the experiments where CO_2 is doubled and SSTs are fixed. As detailed elsewhere (Hansen, 2005), the benefit of using the fixed SST state is that it accounts for fast atmospheric adjustments in N due to increased CO_2, not related to changes in T. However, some surface warming does occur over land in the fixed SST experiments (~0.2 K global mean per doubling of CO_2), so N_{FSST} does not provide a true estimate of $N(T = 0$ K$)$, hence explaining the approximation term used in equation (1).

In some cases, for example, the regional analysis in section 4, when the LE method is not applied, we calculate $-\alpha$ and its radiative components (e.g., $-\alpha_{SWCRE}$, $-\alpha_{LWCRE}$) for P2 and P3 using the same technique as for P1. That is, we calculate the ratio of ΔN (or one of its radiative components) to ΔT for that period and define these delta values by differencing averages at the beginning and end of each period. Specifically, if X is the variable of interest (i.e., T, N, LWCRE, SWCRE, LWCLR, SWCLR), in P2, ΔX_{P2} is defined as the difference between X at the end and beginning of that period, that is, $\Delta X_{P2} = X_{350} - X_{10}$, where X_{10} is the 20 year average between years 1 and 20 and X_{350} is a 100 year average between years 300 and 399. Likewise, ΔX_{P3} is defined as, $\Delta X_{P3} = X_{EQ} - X_{350}$, where X_{EQ} is a 100 year average about the year equilibrium is reached. When $-\alpha$ and other variables are calculated using this method, we will denote it the end point (EP) method.

Control drift is subtracted in all cases using companion preindustrial control simulations of the same length as the 2XS experiment runs (Figure S1 in the supporting information). We use one of two methods to subtract the control, depending upon the analysis performed. For each model, the drift is fitted with a fifth-order polynomial (yellow line, Figure S1). CM3 has a much larger drift than ESM2M, especially during the first 2,000 years (Figure S1). When presenting time series of global mean values in section 3, we use a polynomial to subtract the control drift. However, for the regional analysis in section 4, when the EP method is applied, baseline drift is accounted for by subtracting the equivalent time average in the control run. This is done for two reasons. First, the polynomial fit was found not to be well constrained for individual latitude-longitude points. Second, these control averages are over long enough time periods to make this technique of baseline subtraction produce near identical global mean results to using the polynomial subtraction.

For the analysis in sections 4.3 and 4.4 EIS, in units of Kelvin, is defined by equation 4 of Wood and Bretherton (2006) as

$$\text{EIS} = \text{LTS} - T_{850}(Z_{700} - \text{LCL}), \tag{2}$$

where LTS is the lower-tropospheric stabilty, defined as the difference in potential temperature at 700 mb and at the surface (Klein & Hartmann, 1993), T_{850} is the potential temperature moist adiabat at 850 mb, Z_{700} is the height at 700 mb, and LCL is the lifting condensation level. Hence, EIS is a measure of the difference in potential temperature between the surface and 700 mb plus a correction for the moist adiabat adjustment (assuming this is captured by the moist adiabat calculated at 850 mb) above the LCL.

3. Global Changes

ESM2M simulates T of 3.34 K and N of -0.07 W m^{-2} by year 4300 (assessed as a 200 year average, open circles Figure 1a). CM3 simulates T of 4.84 K and N of -0.09 W m^{-2} by year 4700 (Figure 1b). For ESM2M, T reaches 3.34 K by year 2500, after which it remains almost constant for the remaining 2000 years. To avoid fitting to unforced variability, for the remaining analysis we only apply the LE method until year 2500. In CM3, T steadily increases until year 4700. Therefore, we include the full 4,800 years in our CM3 LE analysis. The reason why warming continues after $N = 0$ W m^{-2} is uncertain. ESM2M first simulates N less than zero (-0.02 W m^{-2}) in year 1700, when T is 3.29 K. CM3 first has an N less than 0 W m^{-2} in year 2900 (-0.01 W m^{-2}) when T is 4.70 K. Because both GCMs reach a state of constant T with negative N, we consider the true ECS defined by this stable state rather than $N = 0$ W m^{-2}. By definition, the LE method estimates ECS as T when $N = 0$ W m^{-2} and therefore a perfect fit will underestimate the true ECS by ~1.5% (0.05 K) for ESM2M and by ~3% for CM3 (0.14 K).

The ECS estimated by applying the LE method to the first 150 years of the 4XI runs (blue crosses in Figures 1c and 1d, 2.4 K ESM2M, 4.0 K CM3 from (Andrews et al., 2012) fails to predict the 2XS ECS and is biased relative to the true ECS by ~15–25%. Yet Figures 1c and 1d show a near-linear relationship between N and T for the 2XS runs. Indeed, the LE method when applied to 4,800 years of CM3 and 2,500 years of ESM2M (Table S1) gives R^2 values of 0.90 and 0.86, respectively. Accordingly, when applied to only the first 150 years (black and red points, Figure 1) after CO_2 is fixed in the 2XS runs, the method performs better than in the 4XI case, although it still results in an underestimate of 8–12%, predicting an ECS of 3.06 K and 4.27 K for ESM2M and CM3, respectively (Figures 1c and 1d and Table S1). Improved ECS estimates of 3.19 K and 4.63 K (both within 5% of the true ECS) can be obtained by fitting to years 51–350 (red and green points, Figure 1). We found that fitting to longer or different periods provided only minimal improvements (<0.1 K) to these estimates.

An informative way to view progress to equilibrium is to plot percent to equilibrium in N versus percent to equilibrium in T (Figures 1e and 1f). This highlights how much changes in N and T are removed from a 1:1 line that would represent a constant $-\alpha$ at all times. We also investigate if the 4XI runs follow a similar pathway to the 2XS if the assumption is made they have twice the equilibrium T of the 2XS runs.

Figure 1e shows that by the end of period 1 (10 years after CO_2 doubling), ESM2M is 43% to equilibrium in T, but 72% to equilibrium in N. This implies that ESM2M has a far larger magnitude $-\alpha$ value (-2.0 W m^{-2} K^{-1}) during the time when CO_2 is increasing (in period 1) compared to the years when the model is under fixed forcing (~-0.6 W m^{-2} K^{-1}, in periods 2 and 3). Therefore, ESM2M never follows the 1:1 line, which represents a fixed $-\alpha$ value of -1.21 W m^{-2} K^{-1} from forcing to equilibrium. For the 2XS run the LE method provides a reasonably accurate estimate of ECS simply by virtue of $-\alpha$ being near constant once CO_2 is constant. However, in the 4XI run, for the first ~50 years there is a substantial adjustment away from the 1:1 line to follow the 2XS case, indicating a changing $-\alpha$ that will influence the accuracy of the LE method (also see Figure S2 for 4XI N versus T plot and values in Table S2).

Figure 1f shows that CM3 behaves similarly to ESM2M and is 47% to equilibrium in T and 68% in N by the end of P1. However, during this initial period CM3 warms more than ESM2M (2.3 K versus 1.4 K) and exhibits a smaller magnitude $-\alpha$ (-1.1 W m^{-2} K^{-1} versus -2.0 W m^{-2} K^{-1}). This difference in $-\alpha$ during P1 while CO_2 is increasing in the 2XS simulations accounts for 0.9 K of the 1.5 K difference in ECS between the two models. Most of the remaining difference is due to CM3 having a smaller magnitude $-\alpha$ (-0.51 W m^{-2} K^{-1} versus -0.56 W m^{-2} K^{-1}) as it heads toward equilibrium and being slightly more out of balance at the end of period 1 (1.2 versus 1.0 W m^{-2}). The eleven 10 year 4XI ensemble members show that CM3 starts quite near the 1:1 line, while the longer 300 year 4XI run shows curvature in T and N space toward the 2XS run.
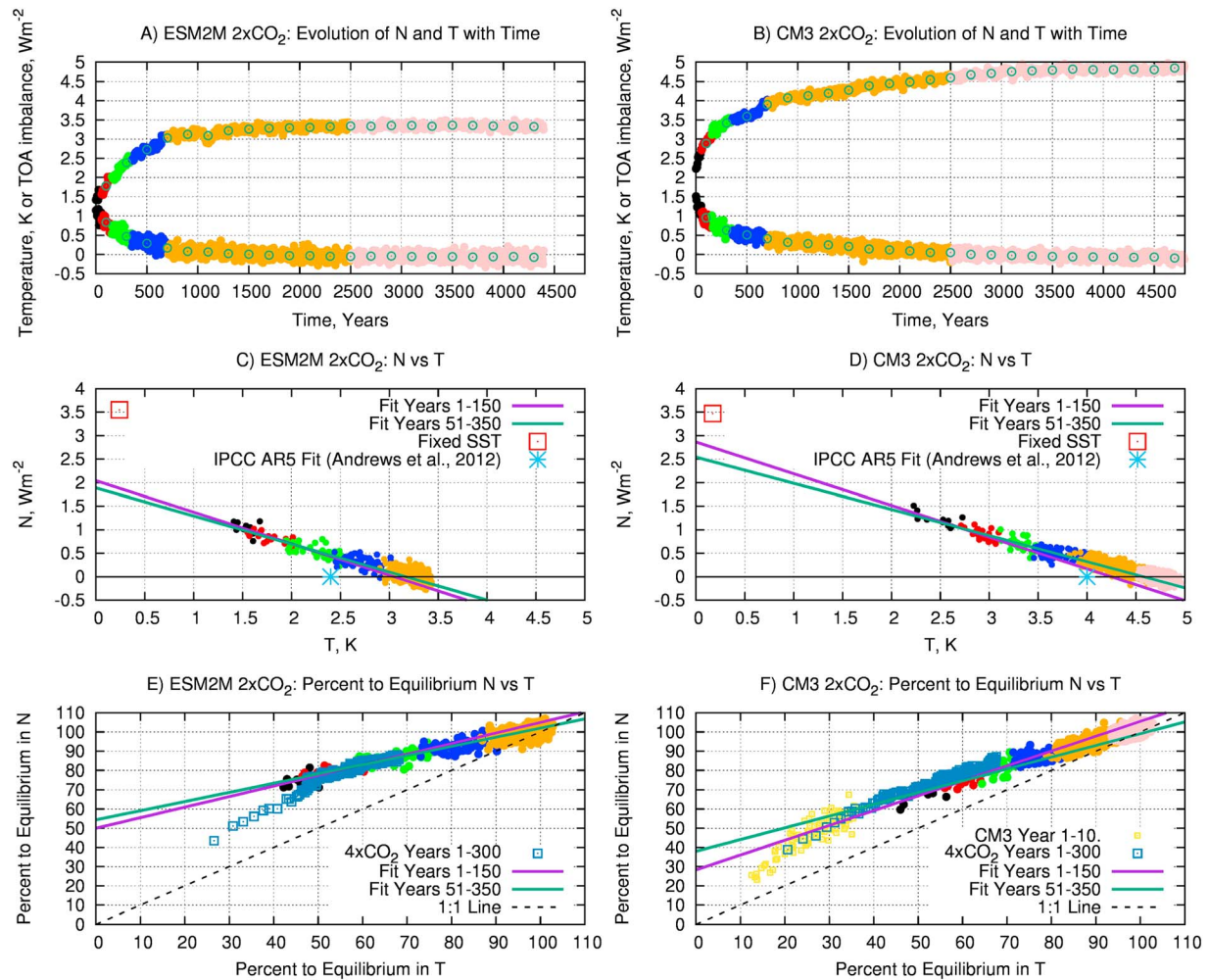
Figure 1. T and N (each filled circle is a 5 year average and clear circle a 200 year average) for years since CO_2 is fixed in the 2XS experiments of ESM2M (a) and CM3 (b). N plotted against T (5 year averages) is shown for ESM2M (years 1–2500) (c) and CM3 (d). The LE method applied to years 1–150 and years 51–350 is shown along with the LE method estimates of ECS from the 4XI experiments published in Andrews et al. (2012) that were used in IPCC-AR5. Percent to equilibrium in N (i.e., $N(T = 0 \text{ K})$ to $N(T = \text{ECS})$) versus percent to equilibrium in T (i.e., $T = 0$ to ECS) are plotted for ESM2M (e) and CM3 (f). Color code for 2XS runs in all panels: Period 2: black (years 1–50), red (years 51–150), green (years 151–350). Period 3: blue (years 351–700), orange (years 701 to 2500), pink (years 2501–4800).

Our results demonstrate that the LE method can be applied to the 4XI runs to produce better predictions of ECS than those in IPCC-AR5, provided the initial years (at least the first 20, preferably 50; see Table S2) when $-\alpha$ changes are discounted. However, even when the LE method was applied to years 101–300, it still estimated low ECS values of 4.3 K and 3.1 K for CM3 and ESM2M, respectively (Table S2). This is in agreement with Armour (2017), where it was found applying the LE method to years 21–150 of a 4XI run of CM3 results in an ECS estimate of 4.3 K. Proistosescu and Huybers (2017) applied a Bayesian statistical method to the first 150 years of 4XI runs to attempt to account for uncertainty in ECS due to decreasing $-\alpha$, but this more advanced method also resulted in an underestimate of ECS for both CM3 (4.1 K) and ESM2M (2.7 K). A similar underestimate was also found for a 4XI run of ESM2M using a different technique of fitting a two box Energy balance model (2.6 K) (Geoffroy, Saint-Martin, Bellon, et al., 2013). Part of the problem appears to be small (~0.1 W m^{-2} K^{-1}) multicentennial changes in $-\alpha$ once CO_2 is fixed, which are not captured by the 300 year length of the 4XI runs. For example, the CM3 $-\alpha$ of -0.6 W m^{-2} K^{-1} for years 101–300 of the 4XI run predicts that the N equals 1.5 W m^{-2} seen in year 300 of the 4XI run will result in 2.5 K further warming. Applying the 2XS $-\alpha$ for period 3 of -0.5 W m^{-2} K^{-1} would instead estimate 3 K further warming.
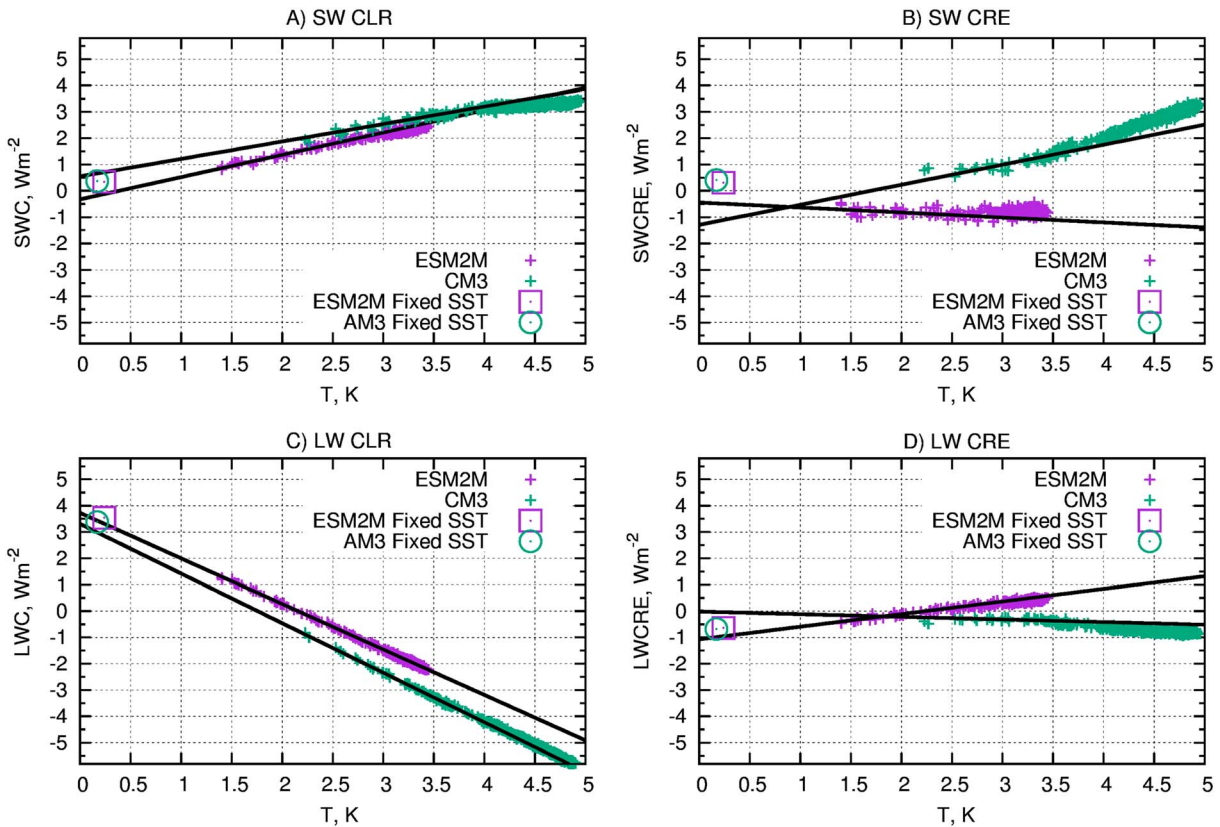
Figure 2. Individual components of N plotted against T for the 2XS runs. The 2xCO$_2$ fixed SST runs are also shown. Lines indicate the fits calculated by the LE method applied to years 51–350 (~P2).

While it is clear that the 2XS runs give more accurate estimates of ECS than the 4XI runs, the question can also be asked whether the 2XS runs are more computationally efficient at reaching the best estimate of ECS achieved by the 300 year 4XI run. In the case of CM3, Table S2 shows that the best estimate of ECS from the 4XI run (4.3 K) is achieved by fitting over years 51–150. This is identical to the estimate produced by fitting to years 1–150 of the 2XS run. In the case of ESM2M the best 4XI estimate of ECS (3.1 K) is achieved by fitting years 101–300, the same value as achieved by fitting to years 1–150 of the 2XS run. Hence, in the case of CM3, the 4XI run is slightly more computationally efficient at reaching the same estimate of ECS (after taking into account that the 2XS case requires 70 years of each an experiment and control run before the LE method can be applied). In the case of ESM2M, the 2XS run is clearly more efficient.

Figure 2 separates N of CM3 and ESM2M into individual radiative components which sum to equal N. This allows the longwave and shortwave clear-sky ($-\alpha_{LWC}$ and $-\alpha_{SWC}$) and cloud radiative effect ($-\alpha_{LWCRE}$ and $-\alpha_{SWCRE}$) to be estimated for different periods, akin to how $-\alpha$ is estimated (Table S3). The cloud radiative effect (CRE) is calculated by calling the radiation code with and without clouds present. Therefore, a change in $-\alpha_{LWCRE}$ or $-\alpha_{SWCRE}$ can result from changes in cloud properties (e.g., optical depth, cloud amount, and overlap) and changes in the properties of the climate system which alter the amount of radiation interacting with clouds (e.g., water vapor, surface albedo, and atmospheric temperature). Our results demonstrates that while CM3 and ESM2M reach the same $-\alpha$ in P2 and P3, they do so through very different contributions from these individual components. The key differences are in $-\alpha_{LWCRE}$ and $-\alpha_{SWCRE}$. We have applied the LE method to years 51–350 (i.e., the time period seen best for estimating ECS ~P2), to see if there are longer term nonlinearities in these individual components. For ESM2M the individual components are largely linear to equilibrium, with perhaps a small upturn in SWCRE at 2.5 K of warming. CM3 on the other hand has a distinct shift when 3.5 K of warming is reached. This change occurs around year 350 (i.e., the transition from P2 to P3) and is highlighted by an increase in $-\alpha_{SWCRE}$, which is almost perfectly balanced by a decrease in $-\alpha_{LWCRE}$
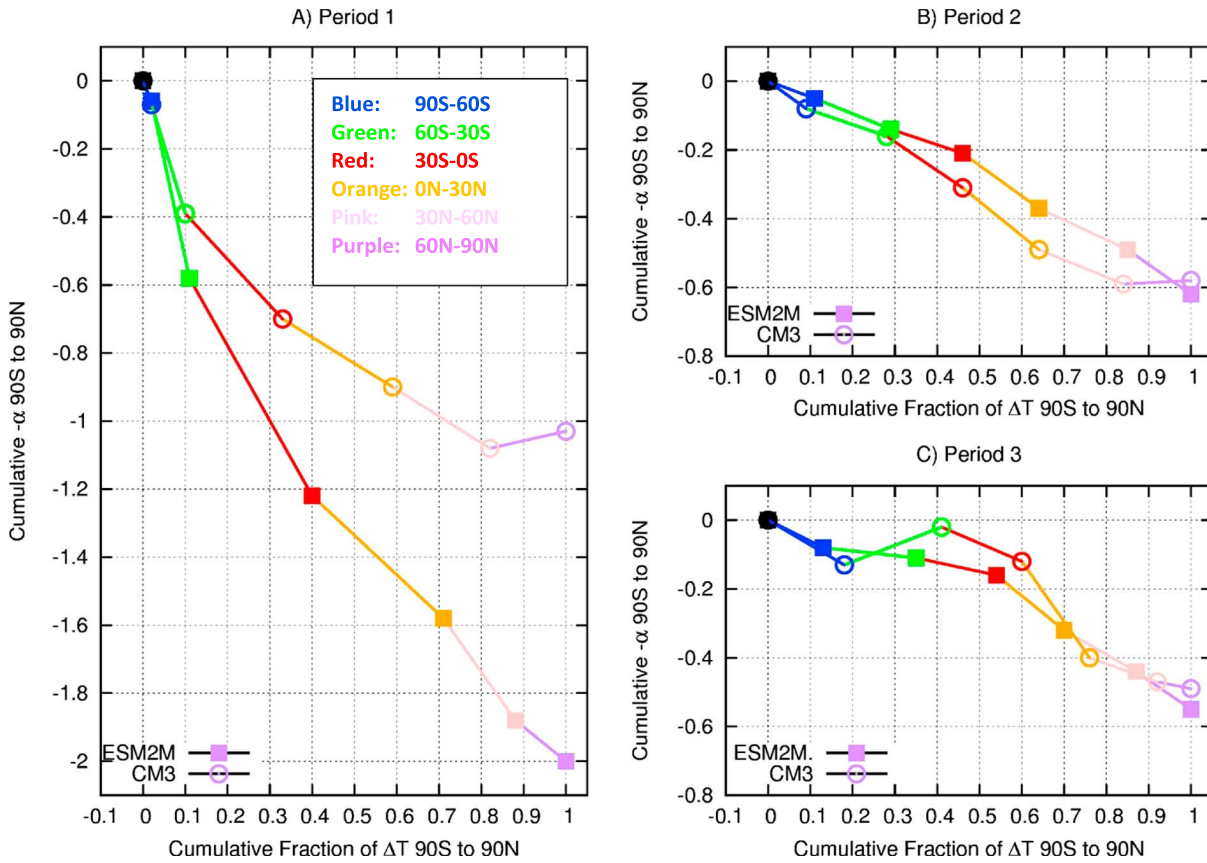
Figure 3. The cumulative change in $-\alpha$ (y axis) versus cumulative change in fraction of ΔT (x axis), integrated from the South Pole to the North Pole for each period. Each point represents the cumulative value up to each 30° latitude region. The change in y axis values between each pair of consecutive points represents the contribution from that latitude region to global $-\alpha$. Thus, the slope between each pair of points represents $-\alpha_k$ of that region (see equation (4)). For example, green points represent the cumulative values at 30°S and the green line $-\alpha_{60S-30S}$. The panels are sized to make $-\alpha_k$ comparable between them. Color code: cumulative value at 90°S—black (always zero), at 60°S—blue, 30°S—green, equator—red, 30°N—orange, 60°N—pink, 90°N—purple.

and $-\alpha_{SWCLR}$. Hence, the linear behavior seen in $-\alpha$ between P2 and P3 (i.e., years 10–4500) is actually due to canceling nonlinear contributions. We discuss the magnitude and causes of these nonlinearities in more detail in the next section.

4. Regional Changes

4.1. The Large-Scale Regional Contributions to $-\alpha$

Following Armour et al. (2013) the area weighted contribution of an arbitrary longitude-latitude point (i,j) to $-\alpha$ is a function of both the regional warming $T_{i,j}$ and the regional feedback parameter value ($-\alpha_{i,j}$, defined as the ratio of $\Delta N_{i,j}$ to $\Delta T_{i,j}$):

$$-\alpha = \sum_{i=1}^{N_{lon}}\sum_{j=1}^{N_{lat}} -\alpha_{i,j}\frac{\Delta T_{i,j}}{\Delta T}w_{i,j} = \sum_{i=1}^{N_{lon}}\sum_{j=1}^{N_{lat}}\frac{\Delta N_{i,j}}{\Delta T_{i,j}}\frac{\Delta T_{i,j}}{\Delta T}w_{i,j} = \frac{1}{\Delta T}\sum_{i=1}^{N_{lon}}\sum_{j=1}^{N_{lat}}\Delta N_{i,j}w_{i,j}, \qquad (3)$$

where global values are denoted by the lack of subscript and $w_{i,j}$ is an area weighting which sums to unity over the whole globe. To apply equation (3) to periods 1–3, we use the End Point method (see section 2). To understand which regions are contributing to $-\alpha$, we split the planet into six large-scale regions, each of 30° latitude. We thus calculate $-\alpha$ from the zonal mean contributions as,

$$-\alpha = -\sum_{k=1}^{6}\alpha_k\frac{\Delta T_k}{\Delta T}w_k, \qquad (4)$$

where the k index refers to each 30° latitude region, numbered consecutively from 90°S to 90°N. We plot (Figure 3) the cumulative contributions to $-\alpha$, that is, $-\sum_{k=1}^{6} \alpha_k \Delta T_k w_k / \Delta T$, against the cumulative contribution to ΔT, that is, $\sum_{k=1}^{6} \Delta T_k w_k / \Delta T$. This allows us to determine which regions contribute most to $-\alpha$ (change in the y value between two latitude points) and whether this contribution is due to local temperature change (change in the x value between two latitude points) or the value of $-\alpha_k$ (the slope of the line between two latitude points). For example, the total contribution to $-\alpha$ from 30°N–60°N in Figure 3a is shown by the difference in y axis values between the orange and pink points. While the difference in x axis values is the between 30°N–60°N contribution of $\Delta T_k / \Delta T$ and gradient of the pink line $-\alpha_{30N\_60N}$.

Studies have highlighted two, nonmutually exclusive ways in which regional changes can alter $-\alpha$. First, a change in the warming pattern (i.e., $\Delta T_k / \Delta T$ in equation (3)) can place different weights on $-\alpha_k$, with the $-\alpha_k$ values themselves remaining constant (Armour et al., 2013). Second, the change in warming pattern can implicitly alter the values of $-\alpha_k$ (Andrews et al., 2015; Good et al., 2015; Paynter & Frölicher, 2015; Rose et al., 2014). Our results in Figure 3 show that the decrease in the magnitude of $-\alpha$ from period 1 to period 2 results largely from changes in $-\alpha_k$ (gradient of the slope between points) rather than changes in the weight each region contributes to ΔT (distribution of points along the x axis). If the $-\alpha_k$ values from period 1 were to remain constant across periods 2 and 3, then $-\alpha$ would actually increase rather than decrease in magnitude. Despite both models reaching similar $-\alpha$ values in periods 2 and 3 (hence the success of the LE method), it is interesting to see, especially for CM3, that the regional contributions vary substantially. For instance, in CM3 during period 3, $-\alpha_k$ for 60–30°S (green segments in Figure 3c) actually becomes positive, while $-\alpha_k$ for 0–30°N (orange segment) increases in magnitude compared with period 2. In the next section we seek to understand more details about the spatial structure and radiative components that lead to these differences seen between the models and periods in Figure 3.

4.2. The Spatial Structure of $-\alpha$

In Figures 4a–4f we show the spatial pattern of $\Delta T_{i,j}$ for ESM2M and CM3. For both GCMs the main difference between the periods is the shift from the majority of the warming being over land, high northern latitudes and over the tropical ocean in P1 to being over the middle and high latitudes in both hemispheres in P2 and P3. The geographic pattern of the contribution to $-\alpha$ (i.e., $\Delta N_{i,j}/\Delta T$ in equation (3)) that results from these different warming patterns is also shown in Figure 4. A positive value of $-\alpha$ or $\Delta N_{i,j}/\Delta T$ indicates increased downward flux and thus a positive radiative feedback. The global mean values (i.e., $-\alpha$) are shown in the figure subtitles. Most of our discussion will focus on changes over tropical and midlatitude oceans in SWCRE and LWCRE. This focus should not imply that the polar regions or clear-sky terms are not also important. Rather, looking at the regions that make the most significant contributions to the changes in $-\alpha$ allows the discussion to be more focused. The reader interested in the contribution to $-\alpha$ from all regions may find Table S4 useful, in which we split the contribution for each period into all land, polar ocean, midlatitude ocean, and tropical ocean regions. We also note that values in this section are calculated with the EP method. For periods (P2 and P3) where both the LE and EP methods have been applied the results are near identical, which can be seen by comparing the captions in Figures 4, 5, and S5 (EP method) with values in Tables S1 and S3 (LE method).

Differences in $\Delta N_{i,j}/\Delta T$ shown in Figure 4 are primarily driven by similarly large changes in the contribution from the respective spatial patterns of $\Delta SWCRE_{i,j}/\Delta T$ and $\Delta LWCRE_{i,j}/\Delta T$ (Figure 5) (for i,j quantities the normalization by ΔT (global mean temperature change) can be assumed in the proceeding text but will be dropped for ease of notation).

In P1, ESM2M has a considerably larger magnitude of $-\alpha$ than CM3 (-2.0 W m^{-2} K^{-1} versus -1.0 W m^{-2} K^{-1}, values from Figure 4), exhibiting a greater negative contribution from nearly all ocean regions (compare Figures 4g and 4j). Globally, of the components contributing to $-\alpha$ in P1, the most significant difference between the models is the $+1.0$ W m^{-2} K^{-1} difference in $-\alpha_{SWCRE}$ (-0.9 W m^{-2} K^{-1} ESM2M versus $+0.2$ W m^{-2} K^{-1} CM3, Figures 5a and 5d), much larger than those associated with the other terms (<0.3 W m^{-2} K^{-1}; Figures 5 and S4). This is mainly related to ESM2M having a strongly negative $\Delta SWCRE_{i,j}$ pattern in numerous midlatitude and tropical ocean regions (Figuere 5d and Table S4). In these same regions, CM3 (Figure 5a and Table S4) either exhibits positive $\Delta SWCRE_{i,j}$ (e.g., the northwest Atlantic Ocean) or weaker negative $\Delta SWCRE_{i,j}$ values (e.g., the Southern Ocean) than ESM2M. However, in some tropical regions, such as
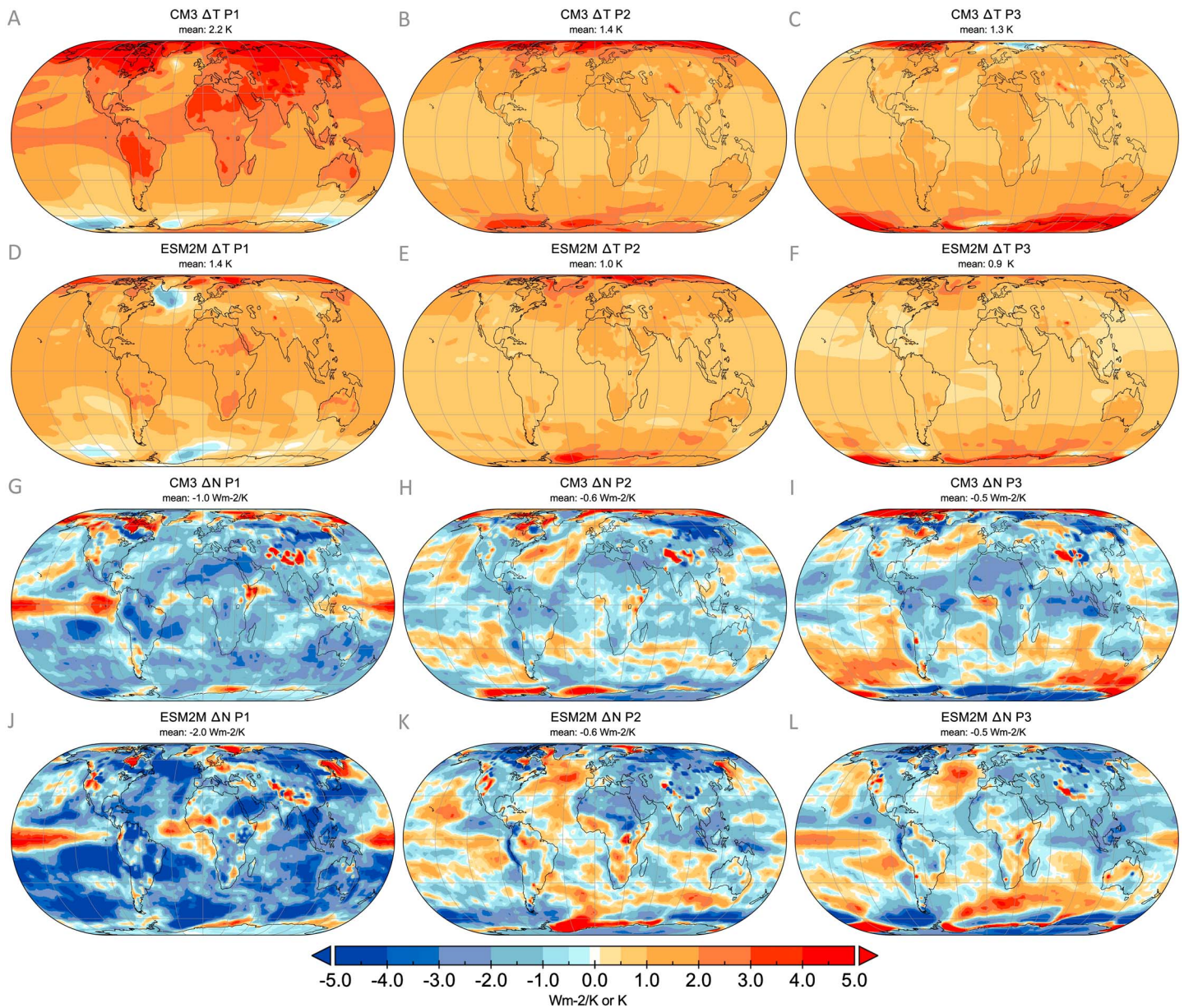
Figure 4. The pattern of $\Delta T_{i,j}$ in each of the periods for CM3 (a–c) and ESM2M (d–f). The panel subtitles show the global mean value of ΔT for each period. The corresponding pattern of $\Delta N_{i,j}/\Delta T$ for each period is shown for CM3 (g–i) and ESM2M (j–l). The global mean of $\Delta N/\Delta T$ (i.e., $-\alpha$) is shown in the figure subtitles. All values are calculated with the end point method.

the Indian Ocean and Indonesian warm pool, areas of negative $\Delta SWCRE_{i,j}$ in ESM2M are canceled out by opposing $\Delta LWCRE_{i,j}$ values (Figure 5g). In fact, the tropical ocean region contribution to $-\alpha$ from the ΔCRE ($\Delta SWCRE + \Delta LWCRE$) in ESM2M is only slightly negative (Table S4, -0.1 W m^{-2} K^{-1}). CM3 does not have a similar cancelation in the tropics between $\Delta LWCRE$ and $\Delta SWCRE$ (Figures 5a and 5g), both remain positive, resulting in the contribution to $-\alpha$ over tropical oceans from the CRE of $+0.4$ W m^{-2} K^{-1} (Table S4). In summary, of the 1.0 W m^{-2} K^{-1} difference in $-\alpha$ between the models in P1, roughly half is due to the aforementioned difference in the tropics and half is due to a stronger negative SWCRE seen over midlatitude oceans in ESM2M (Table S4).

In P2 (years 11–350), ESM2M and CM3 have quite similar $-\alpha$ values (~-0.6 W m^{-2} K^{-1}). Likewise, in P2 both exhibit somewhat similar patterns of $\Delta N_{i,j}$ (Figures 4h and 4k), with weaker negative, and even some positive,
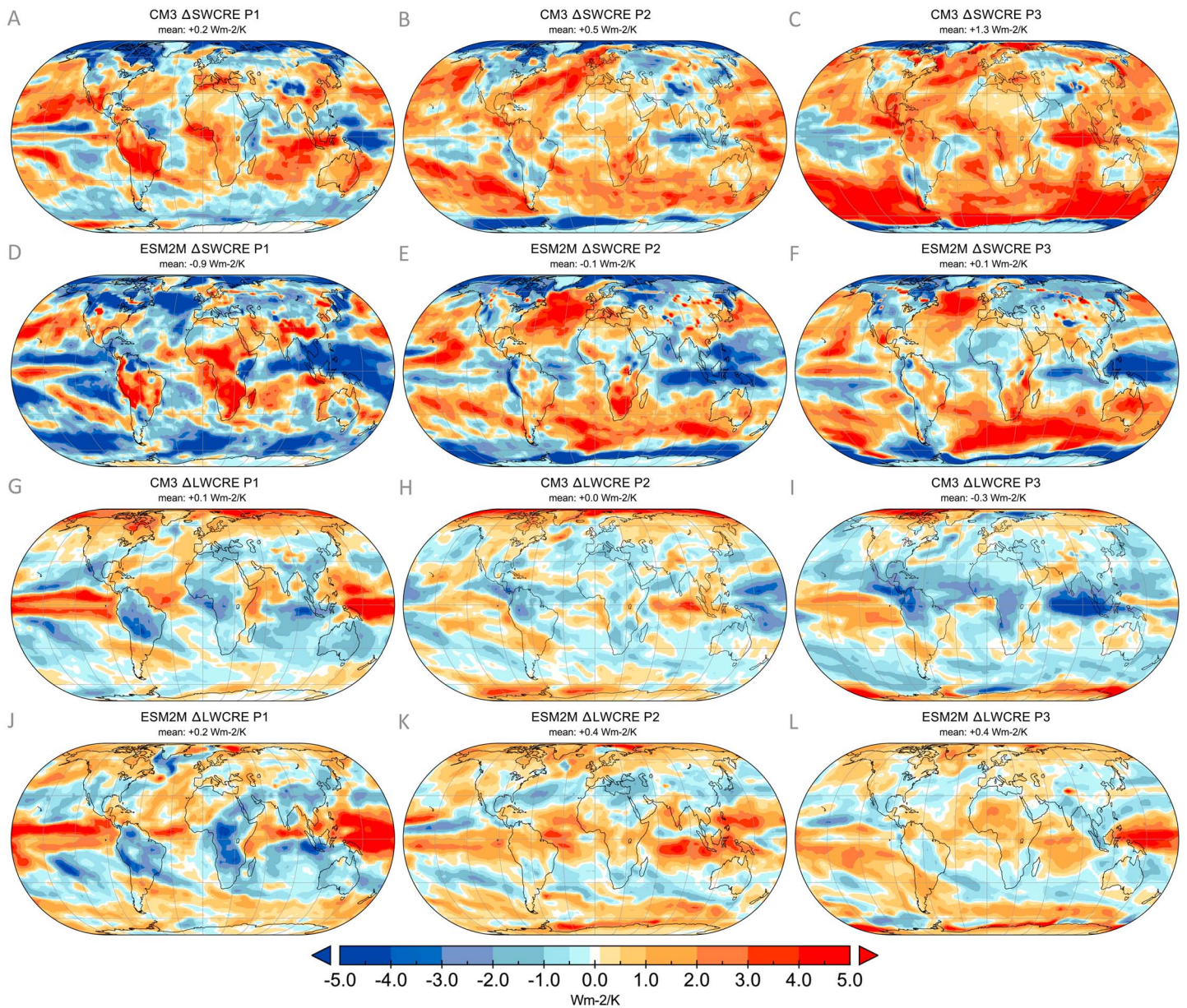
Figure 5. The change in $\Delta SWCRE_{i,j}/\Delta T$ for CM3 (a–c) and ESM2M (d–f), (where ΔT is the global mean surface air temperature change for the associated period). The same is shown for $\Delta LWCRE_{i,j}/\Delta T$ (g–l). The global mean change in $\Delta SWCRE/\Delta T$ (i.e., $-\alpha_{SWCRE}$) or $\Delta LWCRE/\Delta T$ (i.e., $-\alpha_{LWCRE}$) is shown in the figure captions. All values are calculated using the end point method detailed in the text.

values (e.g., areas of the north Atlantic and Southern Ocean) compared to P1. In nearly all ocean regions, CM3 tends to have a uniformly positive $\Delta SWCRE_{i,j}$ (Figure 5b). The same is also the case for ESM2M in the midlatitudes, but over much of the Indian Ocean and western Pacific ESM2M exhibits a negative $\Delta SWCRE_{i,j}$ that was also seen in P1 (Figure 5e). These two negative regions canceling out the positive $\Delta SWCRE_{i,j}$ elsewhere in the tropics and midlatitudes are key to ESM2M having a of near zero $-\alpha_{SWCRE}$ (-0.1 W m^{-2} K^{-1}). In CM3, the Indian Ocean and western Pacific have opposite signs of $\Delta SWCRE_{i,j}$ and thus overall the positive values of $\Delta SWCRE_{i,j}$ in the subtropical and midlatitude oceans dominate, resulting in a positive global $-\alpha_{SWCRE}$ ($+0.5$ W m^{-2} K^{-1}). The strong cloud response in the tropics of ESM2M compared to CM3 also lead to it having larger regions of positive $\Delta LWCRE_{i,j}$, resulting in $-\alpha_{LWCRE}$ of $+0.4$ W m^{-2} K^{-1} compared to 0.0 W m^{-2} K^{-1} (compare Figures 5h and 5k). Thus, despite ESM2M and CM3 having very different patterns of $\Delta SWCRE_{i,j}$ and $\Delta LWCRE_{i,j}$ in P2, the cancelations between the patterns in
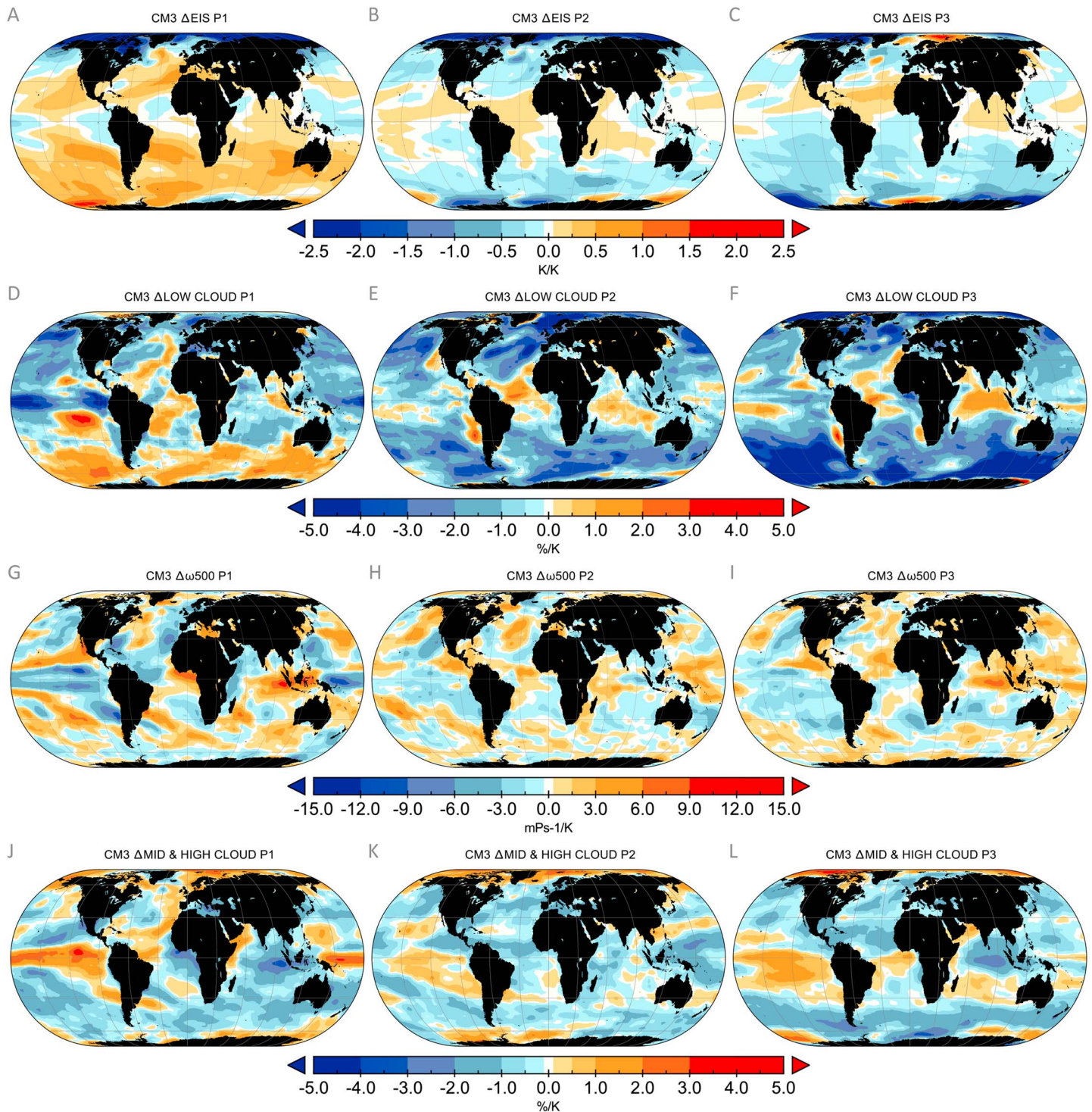
Figure 6. The over ocean change in $\Delta EIS_{i,j}/\Delta T$ (a–c), percentage low cloud amount ($\Delta LC_{i,j}/\Delta T$) (d–e), vertical velocity at 500 mb ($\Delta\omega_{500_{i,j}}/\Delta T$) (g–i), and percentage middle plus high cloud amount ($\Delta MHC_{i,j}/\Delta T$) (j–l) for CM3 for each period. All values are annual averages.

the tropics coupled with both models having positive $\Delta SWCRE_{i,j}$ in the subtropics/midlatitudes result in similar $-\alpha$ values of -0.6 W m^{-2} K^{-1}.

During P3 (year 351 to equilibrium), both models maintain similar $-\alpha$ values to P2. In the case of ESM2M the contribution of the individual $-\alpha$ components also remains largely the same as P2 (Figures 5 and S4). This is

not the case for CM3, which shows decreases in $-\alpha_{SWCLR}$ (from +0.8 to +0.3 W m^{-2} K^{-1}) and $-\alpha_{LWCRE}$ (from +0.0 to -0.3 W m^{-2} K^{-1}) balancing a large increase in $-\alpha_{SWCRE}$ (from +0.5 to +1.3 W m^{-2} K^{-1}). Figure 2 highlights these changes, by showing that the LE method fitted to the individual SWCLR and SWCRE components over years 51–350 (~P2) does badly at predicting future behavior of CM3 in P3. The large increase in $-\alpha_{SWCRE}$ results from an almost universal pattern of positive $\Delta SWCRE_{i,j}$ in P3 (Figure 5c), with the exception of the central tropical Pacific. This strong $\Delta SWCRE_{i,j}$ is somewhat mitigated in the tropics by a corresponding region of negative $\Delta LWCRE_{i,j}$ (Figure 5i) over the Indian Ocean and central Americas. In line with the similar global averages, the $\Delta SWCRE_{i,j}$ and $\Delta LWCRE_{i,j}$ patterns for ESM2M look very similar to P2 (Figures 5f and 5l).

4.3. How Changes in EIS and ω_{500} Relate to Changes in Cloud Radiative Effect

Figures 4 and 5 show that understanding the changes in $-\alpha$ between the models and periods involves decoding a complex pattern of changes in both the $\Delta LWCRE$ and $\Delta SWCRE$. In this section, we investigate if these patterns can be understood by using $\Delta EIS_{i,j}$ and $\Delta \omega_{500i,\,j}$ to represent changes in atmospheric state important for cloud changes. The annual mean patterns of $\Delta EIS_{i,j}$ and $\Delta \omega_{500i,\,j}$ are shown for CM3 (Figure 6) and ESM2M (Figure 7) along with accompanying percentage change in low cloud (defined between 1000–680 mb) amount ($\Delta LC_{i,j}$) and middle plus high cloud (defined between 680 mb and 50 mb) amount ($\Delta MHC_{i,j}$). All four metrics are per kelvin of global mean air temperature change for the respective period (i.e., the same normalization as performed for all results presented previously in section 4.2). We choose low and middle plus high cloud amount to help better understand which clouds and therefore which metric best explains the $\Delta SWCRE_{i,j}$ and $\Delta LWCRE_{i,j}$ patterns of Figure 5.

For both models and over all periods, $\Delta SWCRE_{i,j}$ (Figures 5a–5f) in the extra tropics and midlatitudes is largely related to changes in low cloud amount (Figures 6d–6f and 7d–7f). The salient result is the negative $\Delta LC_{i,j}$ in P2 to P3 and positive $\Delta LC_{i,j}$ in P1 matching the corresponding changes in $\Delta SWCRE_{i,j}$. In the tropics, mainly the $\Delta MHC_{i,j}$ alters $\Delta SWCRE_{i,j}$ and the opposing $\Delta LWCRE_{i,j}$, but there is some mediation from $\Delta LC_{i,j}$, especially for ESM2M in P1 in the tropical stratocumulus regions and over the central Pacific Ocean (e.g., compare Figure 7d to Figure 5d). While we focus on changes in cloud amount, it is important to note that changes in LWCRE and SWCRE are also influenced by changes in other metrics that we do not analyze here, such as cloud optical thickness and cloud height. It is possible that changes in these metrics can offset or reinforce some changes seen in cloud amount.

The key results of Figures 6 and 7 are that the pattern of $\Delta LC_{i,j}$ is predominately captured by that of $\Delta EIS_{i,j}$, and $\Delta MHC_{i,j}$ by that of $\Delta \omega_{500i,\,j}$. Focusing firstly on EIS, in many tropical and midlatitude regions, $\Delta EIS_{i,j}$ shifts from positive in P1 to negative in P2 and P3. In P1 the pattern of $\Delta EIS_{i,j}$ in both models is similar (Figures 6a and 7a), with the strongest increases in $\Delta EIS_{i,j}$ being associated with the stratocumulus regions, but with notable increases over the Southern Ocean and north Atlantic Ocean as well. The main difference between the two models in P1 is that the magnitude of $\Delta EIS_{i,j}$ in ESM2M is greater at some locations. This difference is less apparent in P2 and P3.

For many regions $\Delta EIS_{i,j}$ is a good indicator of the sign and magnitude of $\Delta LC_{i,j}$. This is especially the case for ESM2M in stratocumulus regions (compare Figures 7a and 7d) in P1, confirming previous work (e.g., Grise & Medeiros, 2016; Qu et al., 2015). In P2 and P3 the negative $\Delta EIS_{i,j}$ in large areas of the midlatitudes and subtropics for both models coincides with areas of decreased low cloud amount (Figures 6 and 7b, 7c, 7e, and 7f). These results imply that EIS is a useful metric in many regions for capturing the change in atmospheric state associated with $\Delta SWCRE_{i,j}$ switching from negative to positive between periods (as shown in Figure 5). Hence, it also provides support for the idea that EIS may be a useful metric outside of stratocumulus regions for understanding changes in CRE associated with changes in $-\alpha$ (Rose & Rayborn, 2016; Zhou et al., 2016).

However, over the Southern Ocean in P1 ESM2M and CM3 show a marked and fairly uniformly positive $\Delta EIS_{i,j}$. This is also accompanied in most areas by positive $\Delta LC_{i,j}$, but the areas of strongest $\Delta EIS_{i,j}$ and $\Delta LC_{i,j}$ do not always match up, with the biggest increase in cloud cover being generally to the south of the biggest increase of EIS (compare Figures 6a–6d and 7a–7d). In other regions the sign of $\Delta EIS_{i,j}$ and $\Delta LC_{i,j}$ does not match, for example, the Northern Pacific in P1 for both GCMs and for ESM2M the South Pacific in P2. As we will discuss in the next section, some of these differences can be explained by ΔLC being codependent upon ΔEIS and $\Delta \omega_{500}$.
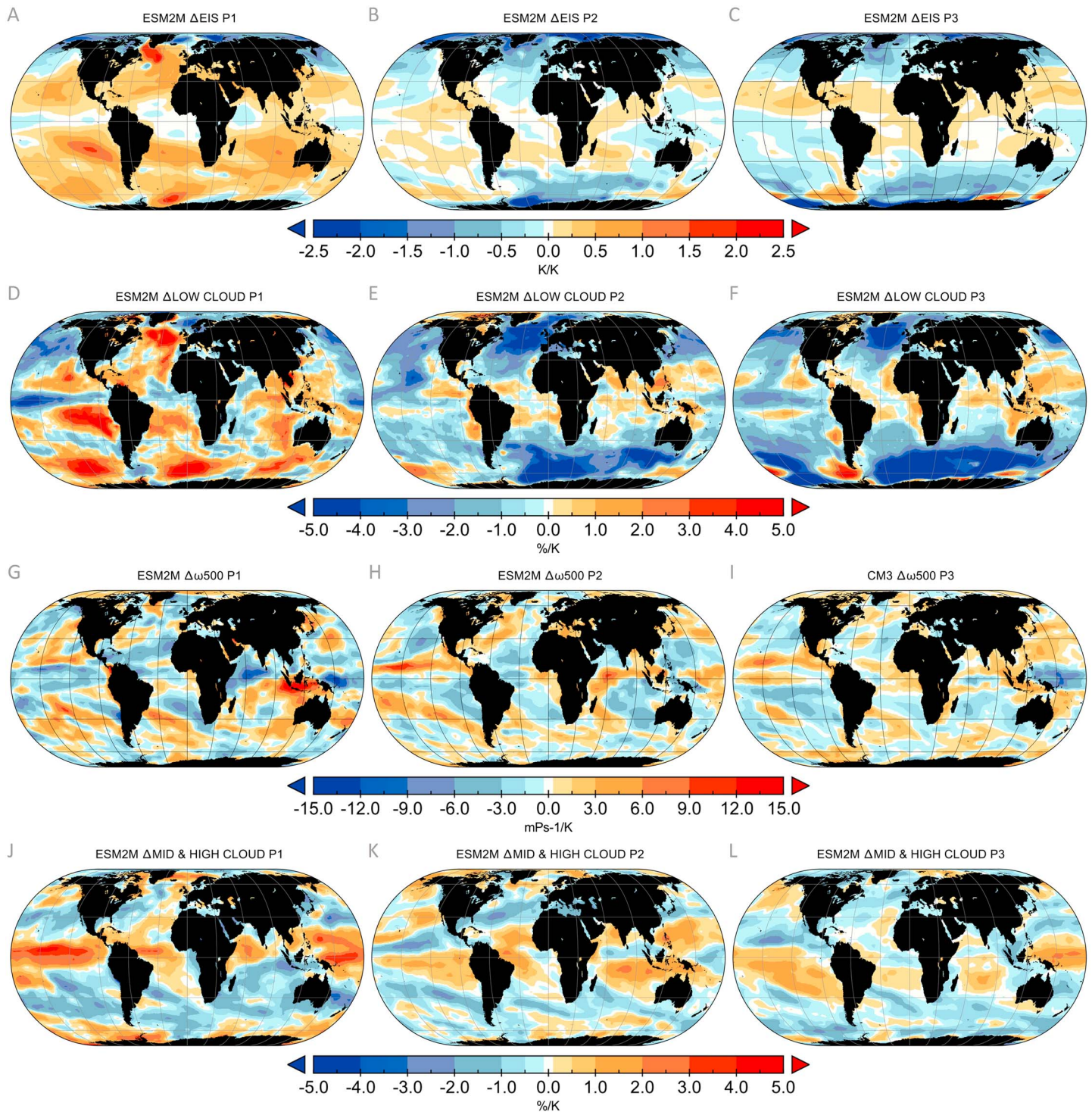
Figure 7. As in Figure 6 but for ESM2M.

In general, $\Delta\omega_{500}$ is a good predictor of both the sign and magnitude of the change of middle plus high cloud in all three periods, which is also consistent with previous work (e.g., Bony et al., 2004; Brient & Bony, 2013; Webb et al., 2015). It captures the key differences seen in $\Delta MHC_{i,j}$ over the Indian Ocean and Pacific warm pool, which can be related to ESM2M favoring more negative $\Delta\omega_{500i,\,j}$ (i.e., increased upward motion) and CM3 more positive $\Delta\omega_{500i,\,j}$ values. Thus, this shows that different strengths of $\Delta SWCRE_{i,j}$ and $\Delta LWCRE_{i,j}$
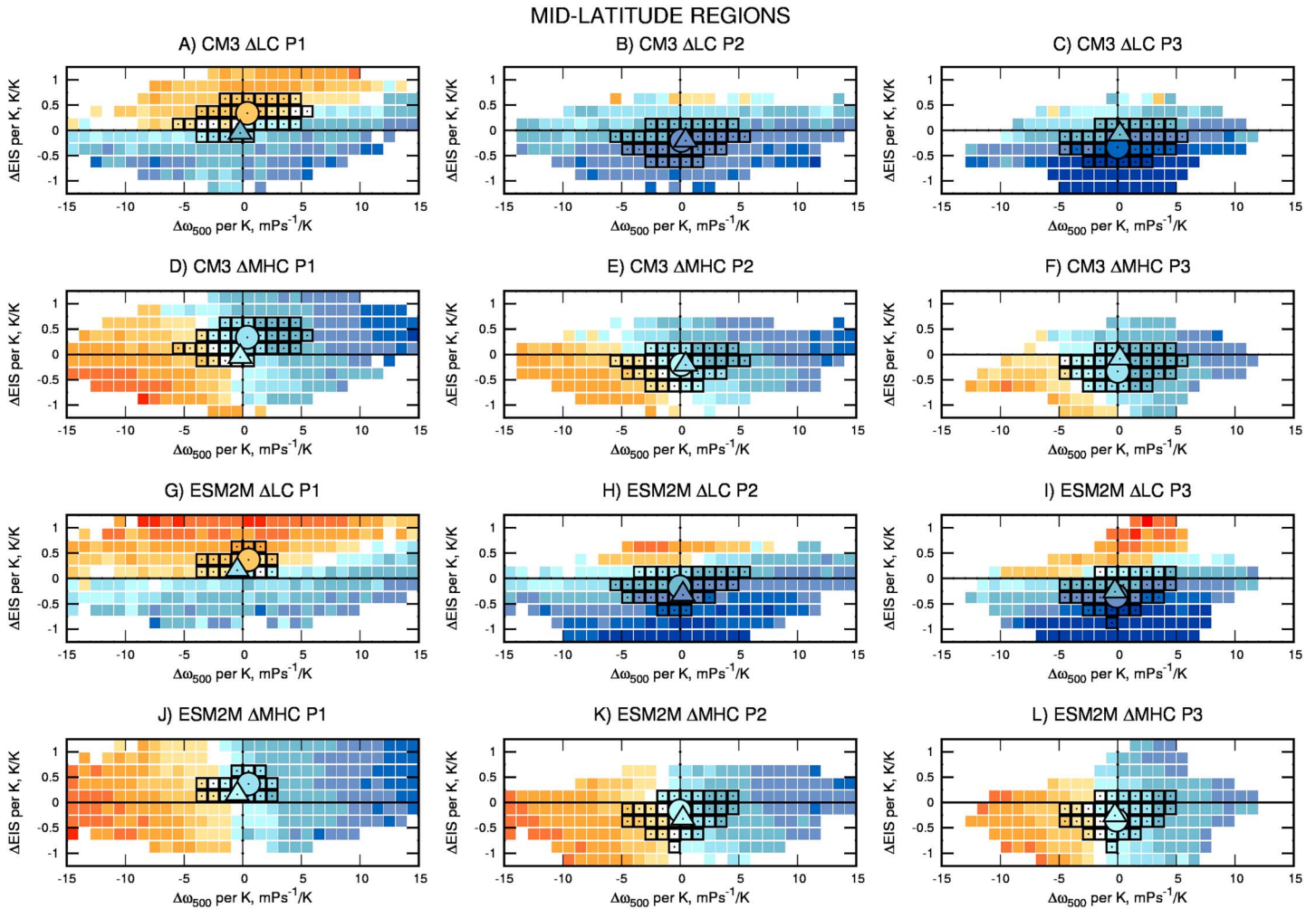
Figure 8. The color of the squares represent the bin averaged monthly percentage change in low cloud cover (a–c) normalized by change in global mean surface air temperature (i.e., $\Delta LC_{i,j}/\Delta T$). These values are binned by $\Delta\omega_{500_{i,j}}/\Delta T$ and $\Delta EIS_{i,j}/\Delta T$ for midlatitude ocean regions (60°S:30°S and 30°N:60°N). The black outlined squares represent bins that occupy more than 1% of the total surface area of this region. The regional mean Northern Hemisphere (triangle) or Southern Hemisphere (circle) values of $\Delta EIS - \omega_{500}$ are shown. The color of the circle or triangle represents the regional mean change in $\Delta LC_{i,j}/\Delta T$. (e–f) The same as (a–c) but for middle plus high cloud (i.e., $\Delta MHC_{i,j}/\Delta T$). (g–l) Same as (a–f) but for ESM2M.

seen in these regions in Figure 5 are associated with differences in the strength of the convective responses between the GCMs. The main region where $\Delta\omega_{500i,\ j}$ works less well is the Southern Ocean in CM3 (Figures 6g–6l) for all three periods, where the $\Delta\omega_{500i,\ j}$ changes are patchy, but the $\Delta MHC_{i,j}$ decrease is near uniform.

4.4. Representing Changes in Cloud Radiative Effect as a Function of $\Delta\omega_{500}$-ΔEIS Space

In the previous section we demonstrated that both $\Delta\omega_{500}$ and ΔEIS are useful, but not perfect, metrics for relating changes in atmospheric state to respective changes in ΔMHC and ΔLC. Latitude-longitude plots make it difficult to quantify and compare the strength of these relationships. Furthermore, they may also hide interesting codependencies of either ΔMHC or ΔLC on both $\Delta\omega_{500}$ and ΔEIS. We propose that one way to better capture the change of atmospheric state between models and between periods is to plot ΔMHC and ΔLC in $\Delta\omega_{500}$-ΔEIS space. We employ a technique similar to that developed by Grise and Medeiros (2016), and for each period, we plot the monthly averaged percent change in cloud amount as a function of binned values of monthly averaged ΔEIS and $\Delta\omega_{500}$. These results are shown in Figures 8 and 9. For each period, we calculate $\Delta\omega_{500i,\ j}$ and $\Delta EIS_{i,j}$ as monthly averages at every i,j point and place these into bins of 1E−3 mbs^{-1} K^{-1} by 0.25 K K^{-1}. For a particular bin, the color represents the average of all of the $\Delta LC_{i,j}$ or $\Delta MHC_{i,j}$ values (in
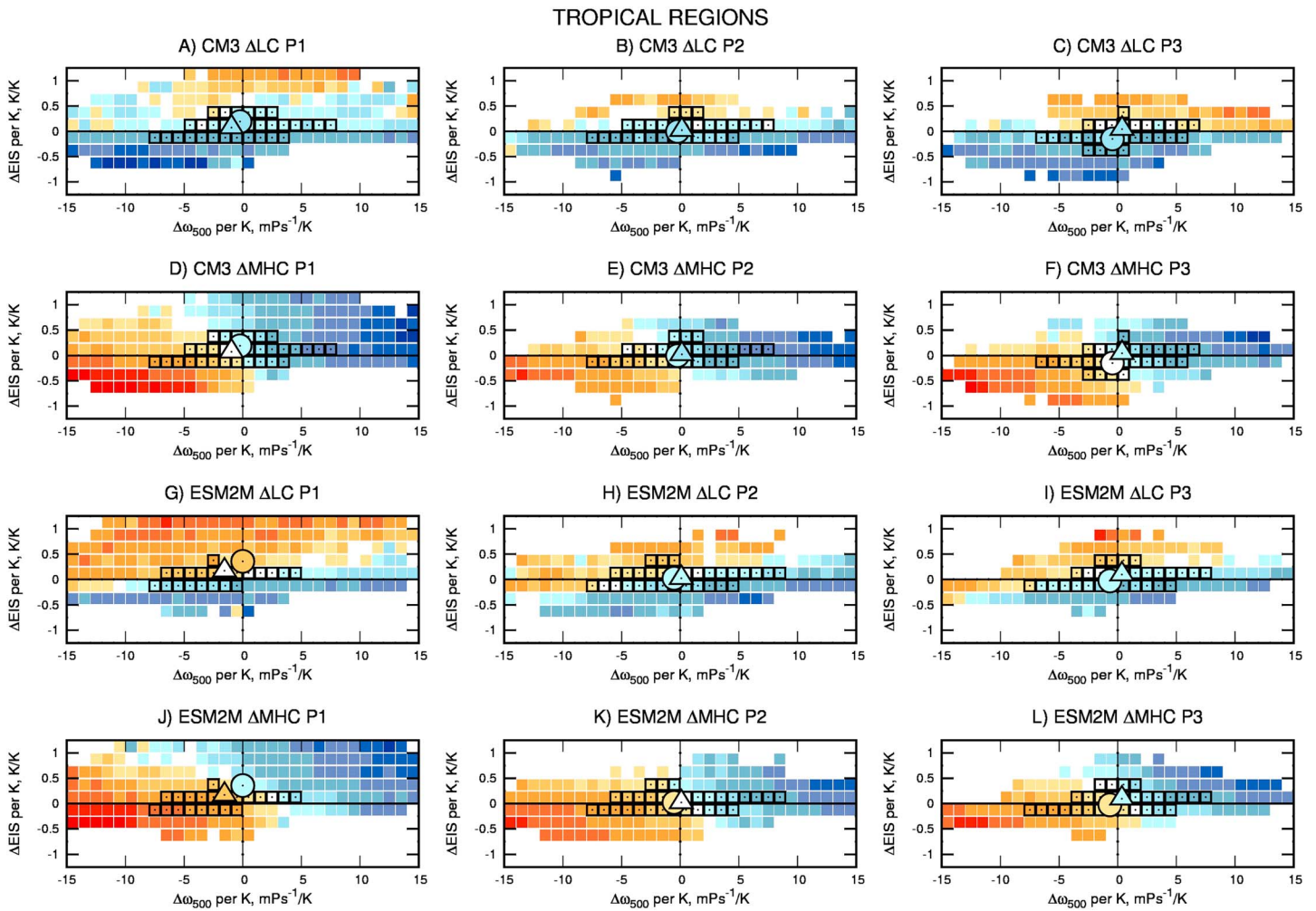
Figure 9. Same as Figure 8 but for the tropical ocean region (30°S:30°N).

units of %K^{-1}) in that bin. However, as it is unclear how many points occupy a particular $\Delta\omega_{500}$-ΔEIS bin, we highlight with black boxes bins that contain more than 1% of the surface area (a more detailed distribution plot is shown in Figure S5). We also plot in the figures the average value of $\Delta\omega_{500}$-ΔEIS for the Northern (triangle) and Southern (circle) Hemispheres, where the color is the regional average change in ΔLC or ΔMHC.

Additionally, $\Delta\omega_{500}$-ΔEIS plots provide a useful visualization to help differentiate between two possibilities: whether a change in cloud amount results from a change in atmospheric state or a difference in cloud response to the same atmospheric state. To demonstrate this, we consider three idealized situations. First, if $\Delta\omega_{500}$-ΔEIS space were a perfect predictor of cloud amount change and made identical predictions for both models, then a particular $\Delta\omega_{500}$-ΔEIS bin in Figure 8 would always have the same change in either low or middle plus high cloud amount associated with it. Therefore, a difference in cloud amount change between models or periods would be the result of a change in the distribution of atmospheric states (e.g., for low cloud, which bins are highlighted in black boxes in Figure 8 would change, but the color of a particular bin would remain the same across Figures 8a–8c and 8g–8i). Therefore, the contribution of cloud amount change to $-\alpha$ would be caused by an atmospheric state change. In the second idealized situation, $\Delta\omega_{500}$-ΔEIS space is a perfect predictor of cloud amount change for each model but differs between models (e.g., for low cloud, the color of a particular bin for Figures 8a–8c would be identical and so would Figures 8g–8i, but Figures 8a–8c and Figures 8g–8i would not be identical to each other). If this were the case, the difference in the contribution of cloud amount change to $-\alpha$ between two models would be the result of different responses of cloud schemes to the same atmospheric state. In the third idealized situation, $\Delta\omega_{500}$-ΔEIS

space is not a perfect predictor for either one of the models (e.g., for low cloud, the color of a particular bin for panels Figures 8a–8c or Figures 8g–8i would be nonidentical). This situation would indicate that cloud amount change is not fully captured by $\Delta\omega_{500}$ and ΔEIS. Hence, ambiguity about which particular changes in the atmospheric state are important for determining the changing cloud amount.

One could expect that the response of both models will to some degree resemble this third idealized response. Clouds in a GCM are ultimately the result of a complex array of 3-D variables; we are attempting to sufficiently capture these variables using only two 2-D proxies. Hence, one aim of our analysis is to determine if any useful predictability results from using $\Delta\omega_{500}$-ΔEIS space (i.e., behavior resembling the first two idealized situations).

Figure 8 does indeed highlight some limitations of using $\Delta\omega_{500}$-ΔEIS space for capturing cloud amount change. Namely, the relationship between $\Delta\omega_{500}$-ΔEIS space and ΔLC or ΔMHC does change for the same model between periods (e.g., compare the ΔLC for same bins between Figures 8a and 8c). Thus, this implies that $\Delta\omega_{500}$-ΔEIS is not fully capturing all of the changes in the atmospheric state related to cloud changes. In addition, the sign of ΔEIS or $\Delta\omega_{500}$ does not always agree with that expected for ΔLC or ΔMHC. For example, in Figure 8c there are bins where ΔLC is negative, even when ΔEIS is positive. The same can also be seen for $\Delta\omega_{500}$ and ΔMHC, where for both models, slightly negative $\Delta\omega_{500}$ values are associated with negative ΔMHC (e.g., Figure 8d). This has implications for the interpretation of the regional mean changes too. For instance, in Figure 8j the average Northern Hemisphere $\Delta\omega_{500}$ (triangle) is negative, but on average ΔMHC decreases.

However, both CM3 and ESM2M exhibit a clear dependence of ΔLC and ΔMHC on $\Delta\omega_{500}$ and ΔEIS that allows us to draw some useful inferences. Most importantly, Figure 8 confirms for both models that the key driver of the change in $-\alpha$ between P1 and P2–P3 (the decrease in low cloud amount over midlatitude oceans) is the result of a change in atmospheric state. Specifically, that the positive midlatitude values of ΔLC in P1 and subsequent negative values in P2 and P3 in both models is accompanied by a shift of ΔEIS from positive to negative. This is shown in Figure 8 by shifts in both the $\Delta\omega_{500}$-ΔEIS bins containing more than 1% of points (i.e., squares with black surround) and also by the regional mean values of $\Delta\omega_{500}$-ΔEIS (circles and triangles).

Figure 8 indicates that for the same ΔEIS and $\Delta\omega_{500}$ state, the two models behave differently, which as discussed above is an indication of the cloud physics schemes responding differently to a similar change in atmospheric state. The key difference is that for positive ΔEIS values, ESM2M increases low cloud more than CM3. Thus, while the distribution of $\Delta\omega_{500}$-ΔEIS space occupied by the models is similar (Figure S5 and black squares in Figure 8), ESM2M increases low cloud more in P1 and decreases it less in P2 and P3 for these states (i.e., behavior similar to that described for the second idealized case). Thereby, this signifies that the more negative values of ΔSWCRE in the midlatitudes (especially in P1) seen in ESM2M compared to CM3 (Figure 5, Table S4) are partially due to differences in the strength of cloud response to a similar change in atmospheric state.

Two key codependencies between $\Delta\omega_{500}$ and ΔEIS are also shown in Figures 8 and 9. First, for the same ΔEIS the strength of the low cloud response is mediated by the strength of $\Delta\omega_{500}$ (perhaps best seen in Figure 8a). A behavior that makes sense in regions where changes in ΔLC are controlled by shallow convection, and therefore $\Delta\omega_{500}$ combined with ΔEIS, might be a better reflection of what changes in the environment impact cloud changes. In the midlatitudes, both models show this behavior (Figure 8). In the tropics (Figure 9) this is not the case for CM3, and ΔLC is largely independent of $\Delta\omega_{500}$. However, at larger magnitudes of $\Delta\omega_{500}$, ΔLC is anticorrelated with ΔMHC.

The first codependence has a bearing upon how regional mean ΔEIS and $\Delta\omega_{500}$ values relate to regional mean changes in cloud amount. For example, in P1, the regional mean Northern Hemisphere ΔLC in ESM2M (triangle, Figure 8g) is negative, but mean ΔEIS is positive and mean $\Delta\omega_{500}$ negative (both indicators of increased low cloud). Similarly, for the Northern Hemisphere in CM3 (triangle, Figure 8a), despite a near-zero mean ΔEIS and $\Delta\omega_{500}$, the mean ΔLC is strongly negative. Both these results can be attributed to the first codependence and specifically bins of positive ΔEIS and $\Delta\omega_{500}$ having negative ΔLC values (best seen in top right quadrant of Figures 8a and 8g). The impact of these anomalous points is that the regional means of ΔEIS and $\Delta\omega_{500}$ may not be such a useful guide to the mean ΔLC.

The second codependence is that the magnitude of ∆MHC is altered considerably by ∆EIS. In general, the more negative ∆EIS values are associated with a greater ∆MHC values and vice versa. This is most likely because ∆EIS is a measure of the stability of the lower atmosphere, and thus, for two atmospheres with identical $\Delta\omega_{500}$, the one with the less stable lower troposphere (i.e., more negative ∆EIS) will see the largest impact on convection and thus the largest cloud changes. Interestingly, both GCMS show this codependence in the tropics (Figure 9), but in the midlatitudes (Figure 8) only CM3 shows this.

There are three key results for the tropics shown in Figure 9 that help us understand the differences in SWCRE and LWCRE between the two models in P1. First, ESM2M for the same positive ∆EIS states has a stronger positive ∆LC response than CM3 and additionally the regional mean ∆EIS values are higher than in CM3 (compare Figure 9a to 9g). This means that on average, ESM2M increases low cloud in the tropics, while CM3 decreases it. Second, ∆LC in the tropics in CM3 is highly anticorrelated with ∆MHC (compare Figure 9a to 9d). This is not the case in ESM2M, where the two are largely independent (compare Figure 9g to 9j). The third result is that CM3 has more negative $\Delta EIS-\Delta\omega_{500}$ states than ESM2M (i.e., in the bottom left quadrant, indicating decreasing ∆LC and increasing ∆MHC). The first result suggests that the large difference in ∆SWCRE between the two GCMs in P1 (Table S4) can be partially explained by the different low cloud response in the tropics. But the second and third allow us to understand how, despite on average having negative ∆LC and ∆MHC, CM3 still has a positive ∆LWCRE averaged over the tropics. This is because replacing low cloud with high cloud will make ∆LWCRE positive but will not significantly alter ∆SWCRE, thus, allowing for the possibility of a positive ∆LWCRE despite an overall decrease in cloud amount. Alternatively, in ESM2M, where middle and high cloud is not replacing low cloud, an increase in tropical middle and high cloud (as is the case in P1) will also lead to an opposing negative ∆SWCRE which counteracts the positive ∆LWCRE. As noted earlier, this ability of CM3 to have additive tropical SWCRE and LWCRE and ESM2M canceling results in 0.5 W m^{-2} K^{-1} of the 1.0 W m^{-2} K^{-1} difference between the GCMs in P1 (Table S4).

For CM3, the tropical contribution from ∆SWCRE and ∆LWCRE to $-\alpha$ in P2 and P3 is largely the same as in P1 (Table S4). This is reflected in the $\Delta\omega_{500}$-∆EIS space occupied between these periods also staying quite similar (Figures 9a–9c). The same largely holds true for ESM2M. However, the key exception is that in both hemispheres, the regional mean ∆EIS shifts from positive (P1) to neutral (P2–P3) (Figures 9g–9i). Thus, in many regions, ∆LC values that were positive in P1 shift negative (which can also be seen in the spatial pattern of ∆LC in Figures 7d and 7f). This is at least partially responsible for the -0.3 W m^{-2} K^{-1} change in the tropical contribution to $-\alpha_{SWCRE}$ in P2 and P3 compared to P1 (Table S4). Through the "second" codependence, a decrease in ∆EIS also alters the ∆MHC response, making ∆MHC greater for the same $\Delta\omega_{500}$. This result may explain how ESM2M is able to keep the same ∆LWCRE (~0.2 W m^{-2} K^{-1}) from the tropics in P1 through P3, despite the regional means of $\Delta\omega_{500}$ being smaller in P2 and P3 compared to P1.

5. Discussion and Conclusions

The fact that $-\alpha$ is almost constant for the majority of the multimillennial 2XS runs allows for highly accurate estimates of ECS by applying the LE method between years 51 and 350. Therefore, a minor modification to the IPCC-AR5 method of obtaining ECS yields improved results for these GCMs. However, we stress that our results are model dependent and other multimillennial GCM runs show changes in $-\alpha$ on longer timescales once CO$_2$ is fixed (Li et al., 2012; Rugenstein, Gregory, et al., 2016) than we see for either of the GCMs investigated here. It is clear from our analysis and other work (Andrews et al., 2015; Gregory & Andrews, 2016; Williams et al., 2008; Winton et al., 2010; Winton, Griffies, et al., 2013) that the evolution of the SST warming pattern is important for determining the evolution of $-\alpha$. Thus, the fact that there is a similar SST warming pattern between P2 and P3 in the case of both models (Figures 4b, 4c, 4e, and 4f) might explain why $-\alpha$ also remains near constant. Meanwhile, the spatial heterogeneity of the SST pattern seen for P1 (Figures 4a and 4d) favors a much larger magnitude of $-\alpha$.

If the evolution of $-\alpha$ is tied to that of the SST pattern, the problem becomes one of understanding how these different patterns lead to such different values of $-\alpha$. Several recent studies have highlighted the importance of cloud processes for understanding the spread in $-\alpha$ between climate models, investigating both the impact of choices made in the convective parameterization (e.g., Bony et al., 2015; Sherwood et al., 2014; Webb et al., 2015; Zhao et al., 2016) and phase partitioning of condensed water in clouds (McCoy et al., 2016; Storelvmo et al., 2015; Tan & Storelvmo, 2015). However, such studies are concerned

with how $-\alpha$ varies between GCMs and generally will represent a single GCM with a single $-\alpha$ value. Our results show that a single GCM can have multiple $-\alpha$ values depending upon the atmospheric state at the time when the GCM is assessed. Additionally, the range in $-\alpha$ for a single GCM is comparable to the spread in $-\alpha$ seen between GCMs. Therefore, when attributing intermodel differences in $-\alpha$ to differences in atmospheric physics parametrizations, the impact of the range of atmospheric states resulting from different SST patterns should also be accounted for.

Plotting ΔEIS and $\Delta\omega_{500}$ demonstrates this significant range of atmospheric states that both GCMs experienced as they progressed toward equilibrium (Figures 6–9). Furthermore, the combination of ΔEIS and $\Delta\omega_{500}$ is useful to differentiate the causes of a change in cloud amount. To first order, a difference in the change in cloud amount between two models for the same ΔEIS and $\Delta\omega_{500}$ state is an indication that their cloud schemes respond differently to a similar atmospheric state. Likewise, a difference in the distribution of ΔEIS and $\Delta\omega_{500}$ states between two models is indicative that the atmospheric state, driven by the SST pattern, is an important factor. This is, of course, an idealized perspective, and our results demonstrated that changes in neither EIS or $\Delta\omega_{500}$ are perfect proxies for the cloud changes seen in either GCM. That considered, we would still argue that plotting the response of a GCM to radiative forcing in ΔEIS and $\Delta\omega_{500}$ space offers significant insight into why two GCMs have a different $-\alpha$ values.

For instance, one of the major differences between the GCMs is that in P1, ESM2M has an $-\alpha$ of -2.0 W m^{-2} K^{-1} and CM3 -1.0 W m^{-2} K^{-1}. In the midlatitudes and tropics ESM2M both increases EIS more and has a greater sensitivity to changes in EIS than CM3 does. This, coupled with a similarly greater sensitivity to decreasing ω_{500} in the Northern Hemisphere tropics, leads ESM2M to have a much stronger increase in both low and middle plus high cloud than CM3 does. Both findings suggest that the most important factor for determining $-\alpha$ in P1 are differences in the atmospheric physics schemes between the two models.

The other main result of this study is the decrease in $-\alpha$ to a very small value (~-0.5–0.6 W m^{-2} K^{-1}) that both GCMs experience in P2 and P3. This decrease can be traced to a decline in atmospheric stability in the midlatitudes, which in turn is associated with decreased low cloud amount. Like in P1, the tropical responses of the models are very different, with ESM2M maintaining a large area of negative $\Delta SWCRE$ associated with increased convection, while CM3 generally decreases both middle plus high and low cloud resulting in mainly positive values of $\Delta SWCRE$. However, despite these extremely different cloud responses, due to cancelation between $\Delta LWCRE$ and $\Delta SWCRE$, both models in P2 and P3 reach a similar near zero ΔCRE contribution from the tropics. Hence, it is the decrease of low clouds in the mid-latitudes that is primarily responsible for the similar $-\alpha$ reached by both models in P2 and P3. This implies that the change in atmospheric state of the midlatitudes, driven by similar SST patterns between the two models, is the most significant factor at play here.

Finally, it is worth considering the possible broader consequences of the results presented here. We briefly consider the implications of the predicted changes in $-\alpha$ seen in both GCMs. The goal of the 2016 Paris Agreement of keeping global warming under 2.0 K requires an estimate of ECS to define an upper limit for carbon emissions. Recent papers have inferred ECS (e.g., Lewis & Curry, 2014; Otto et al., 2013) using present-day observed values of T and N and model-based estimates of F to calculate a value of $-\alpha$ that is assumed to hold constant to equilibrium. This is somewhat akin to assuming that the $-\alpha$ in ESM2M and CM3 for period 1 holds constant to equilibrium, an assumption that underestimates ECS by 1.4 K for both models (Table S1). Future research to understand the physical robustness of the SST pattern, the resulting changes in atmospheric state, and cloud properties that lead to this additional warming is therefore required to reduce uncertainty in observationally inferred estimates of ECS.

References

Andrews, T., Gregory, J. M., & Webb, M. J. (2015). The dependence of radiative forcing and feedback on evolving patterns of surface temperature change in climate models. *Journal of Climate, 28*(4), 1630–1648. https://doi.org/10.1175/JCLI-D-14-00545.1

Andrews, T., Gregory, J. M., Webb, M. J., & Taylor, K. E. (2012). Forcing, feedbacks and climate sensitivity in CMIP5 coupled atmosphere-ocean climate models. *Geophysical Research Letters, 39*, L09712. https://doi.org/10.1029/2012GL051607

Andrews, T., & Webb, M. J. (2017). The dependence of global cloud and lapse-rate feedbacks on the spatial structure of tropical Pacific warming. *Journal of Climate, 31*(2), 641–654, JCLI-D-17-0087.1. https://doi.org/10.1175/JCLI-D-17-0087.1

Armour, K. C. (2017). Energy budget constraints on climate sensitivity in light of inconstant climate feedbacks. *Nature Climate Change, 7*(5), 331–335. https://doi.org/10.1038/nclimate3278

Armour, K. C., Bitz, C. M., & Roe, G. H. (2013). Time-varying climate sensitivity From regional feedbacks. *Journal of Climate*, *26*(13), 4518–4534. https://doi.org/10.1175/JCLI-D-12-00544.1

Armour, K. C., Marshall, J., Scott, J. R., Donohoe, A., & Newsom, E. R. (2016). Southern Ocean warming delayed by circumpolar upwelling and equatorward transport. *Nature Geoscience*, *9*(7), 549–554. https://doi.org/10.1038/ngeo2731

Bony, S., & Dufresne, J. L. (2005). Marine boundary layer clouds at the heart of tropical cloud feedback uncertainties in climate models. *Geophysical Research Letters*, *32*, L20806. https://doi.org/10.1029/2005GL023851

Bony, S., Dufresne, J.-L., Le Treut, H., Morcrette, J.-J., & Senior, C. (2004). On dynamic and thermodynamic components of cloud changes. *Climate Dynamics*, *22*(2-3), 71–86. https://doi.org/10.1007/s00382-003-0369-6

Bony, S., Stevens, B., Frierson, D. M. W., Jakob, C., Kageyama, M., Pincus, R., … Webb, M. J. (2015). Clouds, circulation and climate sensitivity. *Nature Geoscience*, *8*(4), 261–268. https://doi.org/10.1038/ngeo2398

Brient, F., & Bony, S. (2013). Interpretation of the positive low-cloud feedback predicted by a climate model under global warming. *Climate Dynamics*, *40*(9-10), 2415–2431. https://doi.org/10.1007/s00382-011-1279-7

Ceppi, P., & Gregory, J. M. (2017). Relationship of tropospheric stability to climate sensitivity and Earth's observed radiation budget. *Proceedings of the National Academy of Sciences of the United States of America*, *114*(50), 13,126–13,131. https://doi.org/10.1073/pnas.1714308114

Danabasoglu, G., & Gent, P. R. (2009). Equilibrium climate sensitivity: Is it accurate to use a slab ocean model? *Journal of Climate*, *22*(9), 2494–2499. https://doi.org/10.1175/2008JCLI2596.1

Donner, L. J., Wyman, B. L., Hemler, R. S., Horowitz, L. W., Ming, Y., Zhao, M., … Zeng, F. (2011). The dynamical core, physical parameterizations, and basic simulation characteristics of the atmospheric component AM3 of the GFDL global coupled model CM3. *Journal of Climate*, *24*(13), 3484–3519. https://doi.org/10.1175/2011JCLI3955.1

Dunne, J. P., John, J. G., Adcroft, A. J., Griffies, S. M., Hallberg, R. W., Shevliakova, S., … Zadeh, N. (2012). GFDL's ESM2 global coupled climate-carbon earth system models. Part I: Physical formulation and baseline simulation characteristics. *Journal of Climate*, *25*(19), 6646–6665. https://doi.org/10.1175/JCLI-D-11-00560.1

Dunne, J. P., John, J. G., Shevliakova, S., Stouffer, R. J., Krasting, J. P., Malyshev, S. L., … Zadeh, N. (2013). GFDL's ESM2 global coupled climate-carbon earth system models. Part II: Carbon system formulation and baseline simulation characteristics. *Journal of Climate*, *26*(7), 2247–2267. https://doi.org/10.1175/JCLI-D-12-00150.1

Feldl, N., Frierson, D. M. W., & Roe, G. H. (2014). The influence of regional feedbacks on circulation sensitivity. *Geophysical Research Letters*, *41*, 2212–2220. https://doi.org/10.1002/2014GL059336

Flato, G., Marotzke, J., Abiodun, B., Braconnot, P., Chou, S. C., Collins, W., … Rummukainen, M. (2013). Evaluation of Climate Models. In T. F. Stocker, et al. (Eds.), *Climate change 2013: The physical science basis. Contribution of working group I to the fifth assessment report of the intergovernmental panel on climate change* (pp. 741–866). Cambridge, New York: Cambridge University Press.

Frölicher, T. L., & Paynter, D. (2015). Extending the relationship between global warming and cumulative carbon emissions to multi-millennial timescales. *Environmental Research Letters*, *10*(7), 75002. https://doi.org/10.1088/1748-9326/10/7/075002

Frölicher, T. L., Winton, M., & Sarmiento, J. L. (2014). Continued global warming after CO_2 emissions stoppage. *Nature Climate Change*, *4*(1), 40–44. https://doi.org/10.1038/nclimate2060

Geoffroy, O., Saint-Martin, D., Bellon, G., Voldoire, A., Olivié, D. J. L., & Tytéca, S. (2013). Transient climate response in a two-layer energy-balance model. Part II: Representation of the efficacy of deep-ocean heat uptake and validation for CMIP5 AOGCMs. *Journal of Climate*, *26*(6), 1859–1876. https://doi.org/10.1175/JCLI-D-12-00196.1

Geoffroy, O., Saint-Martin, D., Olivié, D. J. L., Voldoire, A., Bellon, G., & Tytéca, S. (2013). Transient climate response in a two-layer energy-balance model. Part I: Analytical solution and parameter calibration using CMIP5 AOGCM experiments. *Journal of Climate*, *26*(6), 1841–1857. https://doi.org/10.1175/JCLI-D-12-00195.1

Gettelman, A., Kay, J. E., & Shell, K. M. (2012). The evolution of climate sensitivity and climate feedbacks in the Community Atmosphere Model. *Journal of Climate*, *25*(5), 1453–1469. https://doi.org/10.1175/JCLI-D-11-00197.1

Good, P., Lowe, J. A., Andrews, T., Wiltshire, A., Chadwick, R., Ridley, J. K., … Shiogama, H. (2015). Nonlinear regional warming with increasing CO_2 concentrations. *Nature Climate Change*, *5*(2), 138–142. https://doi.org/10.1038/nclimate2498

Gregory, J. M., & Andrews, T. (2016). Variation in climate sensitivity and feedback parameters during the historical period. *Geophysical Research Letters*, *43*, 3911–3920. https://doi.org/10.1002/2016GL068406

Gregory, J. M., Ingram, W. J., Palmer, M. A., Jones, G. S., Stott, P. A., Thorpe, R. B., … Williams, K. D. (2004). A new method for diagnosing radiative forcing and climate sensitivity. *Geophysical Research Letters*, *31*, L03205. https://doi.org/10.1029/2003GL018747

Griffies, S. M., Winton, M., Donner, L. J., Horowitz, L. W., Downes, S. M., Farneti, R., … Zadeh, N. (2011). The GFDL CM3 coupled climate model: Characteristics of the ocean and sea ice simulations. *Journal of Climate*, *24*(13), 3520–3544. https://doi.org/10.1175/2011JCLI3964.1

Grise, K. M., & Medeiros, B. (2016). Understanding the varied influence of midlatitude jet position on clouds and cloud radiative effects in observations and global climate models. *Journal of Climate*, *29*(24), 9005–9025. https://doi.org/10.1175/JCLI-D-16-0295.1

Hansen, J. (2005). Efficacy of climate forcings. *Journal of Geophysical Research*, *110*, D18104. https://doi.org/10.1029/2005JD005776

Haugstad, A. D., Armour, K. C., Battisti, D. S., & Rose, B. E. J. (2017). Relative roles of surface temperature and climate forcing patterns in the inconstancy of radiative feedbacks. *Geophysical Research Letters*, *44*, 7455–7463. https://doi.org/10.1002/2017GL074372

He, J., Winton, M., Vecchi, G., Jia, L., & Rugenstein, M. A. A. (2017). Transient climate sensitivity depends on base climate ocean circulation. *Journal of Climate*, *30*(4), 1493–1504. https://doi.org/10.1175/JCLI-D-16-0581.1

Jonko, A. K., Shell, K. M., Sanderson, B. M., & Danabasoglu, G. (2012). Climate feedbacks in CCSM3 under changing CO_2 forcing. Part I: Adapting the linear radiative kernel technique to feedback calculations for a broad range of forcings. *Journal of Climate*, *25*(15), 5260–5272. https://doi.org/10.1175/JCLI-D-11-00524.1

Kay, J. E., Holland, M. M., Bitz, C. M., Blanchard-Wrigglesworth, E., Gettelman, A., Conley, A., & Bailey, D. (2012). The influence of local feedbacks and northward heat transport on the equilibrium Arctic climate response to increased greenhouse gas forcing. *Journal of Climate*, *25*(16), 5433–5450. https://doi.org/10.1175/JCLI-D-11-00622.1

Klein, S. A., & Hartmann, D. L. (1993). The seasonal cycle of low stratiform clouds. *Journal of Climate*, *6*(8), 1587–1606. https://doi.org/10.1175/1520-0442(1993)006%3C1587:TSCOLS%3E2.0.CO;2

Knutti, R., & Hegerl, G. C. (2008). The equilibrium sensitivity of the Earth's temperature to radiation changes. *Nature Geoscience*, *1*(11), 735–743. https://doi.org/10.1038/ngeo337

Knutti, R., & Rugenstein, M. A. A. (2015). Feedbacks, climate sensitivity and the limits of linear models. *Philosophical Transactions of the Royal Society A: Mathematical, Physical and Engineering Sciences*, *373*(2054). https://doi.org/10.1098/rsta.2015.0146

Lewis, N., & Curry, J. A. (2014). The implications for climate sensitivity of AR5 forcing and heat uptake estimates. *Climate Dynamics*, *45*(3-4), 1009–1023. https://doi.org/10.1007/s00382-014-2342-y

Li, C., Storch, J.-S., & Marotzke, J. (2012). Deep-ocean heat uptake and equilibrium climate response. *Climate Dynamics*, *40*(5-6), 1071–1086. https://doi.org/10.1007/s00382-012-1350-z

Marvel, K., Schmidt, G. A., Miller, R. L., & Nazarenko, L. S. (2016). Implications for climate sensitivity from the response to individual forcings. *Nature Climate Change*, *6*(4), 386–389. https://doi.org/10.1038/nclimate2888

McCoy, D. T., Tan, I., Hartmann, D. L., Zelinka, M. D., & Storelvmo, T. (2016). On the relationships among cloud cover, mixed-phase partitioning, and planetary albedo in GCMs. *Journal of Advances in Modeling Earth Systems*, *8*(2), 650–668. https://doi.org/10.1002/2015MS000589

Meraner, K., Mauritsen, T., & Voigt, A. (2013). Robust increase in equilibrium climate sensitivity under global warming. *Geophysical Research Letters*, *40*, 5944–5948. https://doi.org/10.1002/2013GL058118

Murphy, J. M. (1995). Transient response of the Hadley Centre coupled ocean–atmosphere model to increasing carbon dioxide. Part III: Analysis of global-mean response using simple models. *Journal of Climate*, *8*(3), 496–514. https://doi.org/10.1175/1520-0442(1995)008%3C0496:TROTHC%3E2.0.CO;2

Otto, A., Otto, F. E. L., Boucher, O., Church, J., Hegerl, G., Forster, P. M., & R, M. (2013). Energy budget constraints on climate response. *Nature Geoscience*, *6*(6), 415–416. https://doi.org/10.1038/ngeo1836

Paynter, D., & Frölicher, T. L. (2015). Sensitivity of radiative forcing, ocean heat uptake, and climate feedback to changes in anthropogenic greenhouse gases and aerosols. *Journal of Geophysical Research: Atmospheres*, *120*, 9837–9854. https://doi.org/10.1002/2015JD023364

Proistosescu, C., & Huybers, P. J. (2017). Slow climate mode reconciles historical and model-based estimates of climate sensitivity. *Science Advances*, *3*(7), e1602821. https://doi.org/10.1126/sciadv.1602821

Qu, X., Hall, A., Klein, S. A., & Deangelis, A. M. (2015). Positive tropical marine low-cloud cover feedback inferred from cloud-controlling factors. *Geophysical Research Letters*, *42*, 7767–7775. https://doi.org/10.1002/2015GL065627

Rose, B. E. J., Armour, K. C., Battisti, D. S., Feldl, N., & Koll, D. D. B. (2014). The dependence of transient climate sensitivity and radiative feedbacks on the spatial pattern of ocean heat uptake. *Geophysical Research Letters*, *41*, 1071–1078. https://doi.org/10.1002/2013GL058955

Rose, B. E. J., & Rayborn, L. (2016). The effects of ocean heat uptake on transient climate sensitivity. *Current Climate Change Reports*, *2*(4), 1–12, 201. https://doi.org/10.1007/s40641-016-0048-4

Rugenstein, M. A. A., Caldeira, K., & Knutti, R. (2016). Dependence of global radiative feedbacks on evolving patterns of surface heat fluxes. *Geophysical Research Letters*, *43*, 9877–9885. https://doi.org/10.1002/2016GL070907

Rugenstein, M. A. A., Gregory, J. M., Schaller, N., Sedláček, J., & Knutti, R. (2016). Multiannual ocean–atmosphere adjustments to radiative forcing. *Journal of Climate*, *29*(15), 5643–5659. https://doi.org/10.1175/JCLI-D-16-0312.1

Senior, A., & Mitchell, J. (2000). The time-dependence of climate sensitivity. *Geophysical Research Letters*, *27*, 2685–2688. https://doi.org/10.1029/2000GL011373

Sherwood, S. C., Bony, S., Boucher, O., Bretherton, C., Forster, P. M., Gregory, J. M., & Stevens, B. (2015). Adjustments in the forcing-feedback framework for understanding climate change. *Bulletin of the American Meteorological Society*, *96*(2), 217–228. https://doi.org/10.1175/BAMS-D-13-00167.1

Sherwood, S. C., Bony, S., & Dufresne, J.-L. (2014). Spread in model climate sensitivity traced to atmospheric convective mixing. *Nature*, *505*(7481), 37–42. https://doi.org/10.1038/nature12829

Shindell, D. T. (2014). Inhomogeneous forcing and transient climate sensitivity. *Nature Climate Change*, *4*(4), 274–277. https://doi.org/10.1038/NCLIMATE2136

Shindell, D. T., Schulz, M., Ming, Y., Takemura, T., Faluvegi, G., & Ramaswamy, V. (2010). Spatial scales of climate response to inhomogeneous radiative forcing. *Journal of Geophysical Research*, *115*, D19110. https://doi.org/10.1029/2010JD014108

Silvers, L. G., Paynter, D., & Zhao, M. (2017). The diversity of cloud responses to twentieth-century sea surface temperatures. *Geophysical Research Letters*, *45*, 391–400. https://doi.org/10.1002/2017GL075583

Storelvmo, T., Tan, I., & Korolev, A. V. (2015). Cloud phase changes induced by CO_2 warming—A powerful yet poorly constrained cloud-climate feedback. *Current Climate Change Reports*, *1*(4), 288–296. https://doi.org/10.1007/s40641-015-0026-2

Stouffer, R. J., & Manabe, S. (1999). Response of a coupled ocean-atmosphere model to increasing atmospheric carbon dioxide: Sensitivity to the rate of increase. *Journal of Climate*, *12*(8), 2224–2237. https://doi.org/10.1175/1520-0442(1999)012%3C2224:ROACOA%3E2.0.CO;2

Stouffer, R. J., & Manabe, S. (2003). Equilibrium response of thermohaline circulation to large changes in atmospheric CO_2 concentration. *Climate Dynamics*, *20*(7-8), 759–773. https://doi.org/10.1007/s00382-002-0302-4

Tan, I., & Storelvmo, T. (2015). Sensitivity study on the influence of cloud microphysical parameters on mixed-phase cloud thermodynamic phase partitioning in CAM5. *Journal of the Atmospheric Sciences*, *73*(2), 709–728. https://doi.org/10.1175/JAS-D-15-0152.1

Trossman, D. S., Palter, J. B., Merlis, T. M., Huang, Y., & Xia, Y. (2016). Large-scale ocean circulation-cloud interactions reduce the pace of transient climate change. *Geophysical Research Letters*, *43*, 3935–3943. https://doi.org/10.1002/2016GL067931

Webb, M. J., Lambert, F. H., & Gregory, J. M. (2012). Origins of differences in climate sensitivity, forcing and feedback in climate models. *Climate Dynamics*, *40*(3-4), 677–707. https://doi.org/10.1007/s00382-012-1336-x

Webb, M. J., Lock, A. P., Bretherton, C. S., Bony, S., Cole, J. N. S., Idelkadi, A., … Zhao, M. (2015). The impact of parametrized convection on cloud feedback. *Philosophical Transactions. Series A, Mathematical, Physical, and Engineering Sciences*, *373*(2054). https://doi.org/10.1098/rsta.2014.0414

Williams, K. D., Ingram, W. J., & Gregory, J. M. (2008). Time variation of effective climate sensitivity in GCMs. *Journal of Climate*, *21*(19), 5076–5090. https://doi.org/10.1175/2008JCLI2371.1

Winton, M., Adcroft, A., Griffies, S. M., Hallberg, R. W., Horowitz, L. W., & Stouffer, R. J. (2013). Influence of ocean and atmosphere components on simulated climate sensitivities. *Journal of Climate*, *26*(1), 231–245. https://doi.org/10.1175/JCLI-D-12-00121.1

Winton, M., Griffies, S. M., Samuels, B. L., Sarmiento, J., & Frölicher, T. L. (2013). Connecting changing ocean circulation with changing climate. *Journal of Climate*, *26*(7), 2268–2278. https://doi.org/10.1175/JCLI-D-12-00296.1

Winton, M., Takahashi, K., & Held, I. M. (2010). Importance of ocean heat uptake efficacy to transient climate change. *Journal of Climate*, *23*(9), 2333–2344. https://doi.org/10.1175/2009JCLI3139.1

Wood, R., & Bretherton, C. S. (2006). On the relationship between stratiform low cloud cover and lower-tropospheric stability. *Journal of Climate*, *19*(24), 6425–6432. https://doi.org/10.1175/JCLI3988.1

Zhao, M., Golaz, J. C., Held, I. M., Ramaswamy, V., Lin, S. J., Ming, Y., … Guo, H. (2016). Uncertainty in model climate sensitivity traced to representations of cumulus precipitation microphysics. *Journal of Climate*, *29*(2), 543–560. https://doi.org/10.1175/JCLI-D-15-0191.1

Zhou, C., Zelinka, M. D., & Klein, S. A. (2016). Impact of decadal cloud variations on the Earth's energy budget. *Nature Geoscience*, *9*(12), 871–874. https://doi.org/10.1038/ngeo2828

Zhou, C., Zelinka, M. D., & Klein, S. A. (2017). Analyzing the dependence of global cloud feedback on the spatial pattern of sea surface temperature change with a Green's function approach. *Journal of Advances in Modeling Earth Systems*, *9*(5), 2174–2189. https://doi.org/10.1002/2017MS001096